Master's Thesis

Skin-Friction Drag Reduction in a Turbulent Channel Flow based on Wall Shear-Free Control

Jung Hoon Kim

Department of Mechanical Engineering

Graduate School of UNIST

2017

Skin-Friction Drag Reduction in a Turbulent Channel Flow based on Wall Shear-Free Control

Jung Hoon Kim

Department of Mechanical Engineering

Graduate School of UNIST

Skin-Friction Drag Reduction in a Turbulent Channel Flow based on Wall Shear-Free Control

A thesis/dissertation
submitted to the Graduate School of UNIST
in partial fulfillment of the
requirements for the degree of
Master of Science

Jung Hoon Kim

01. 06. 2017 Month/Day/Year of submission

Approved by

_____

Advisor

Jae Hwa Lee

Skin-Friction Drag Reduction in a Turbulent Channel Flow based on Wall Shear-Free control

Jung Hoon Kim

This certifies that the thesis/dissertation of Jung Hoon Kim is approved.

01. 06. 2017 Month/Day/Year of submission

signature

_____

Advisor: Jae Hwa Lee

signature

_____

Chun Sang Yoo: Thesis Committee Member #1

signature

_____

Jooha Kim: Thesis Committee Member #2

signature

_____

typed name: Thesis Committee Member #3

signature

_____

typed name: Thesis Committee Member #4;

three signatures total in case of masters

Abstract

Skin-Friction Drag Reduction in a Turbulent Channel Flow based on Wall Shear-Free Control

Active flow control of wall-bounded turbulent flow for skin-friction drag reduction (DR) has been received great attention in recent years due to large economical and ecological interest. In the present study, direct numerical simulations (DNSs) of turbulent channel flows are utilized to explore an active flow control concept using streamwise shear-free control (SSFC) at the wall. The control is only applied to half of the entire wall comprised of spanwise-alternating longitudinal regions of no-control and control surfaces for simplicity, and the simulations are systematically performed with changing the spanwise periodicity (P/h) of the control surface. In addition, an amplitude parameter (A) imposing the strength of the actuating streamwise velocity at the wall is introduced to enhance the skin-friction DR. Significant DR is observed with increasing the two parameters with accompanying reduction of the Reynolds stresses and vorticity fluctuations, although further increase of the parameters amplifies the turbulence activity in the near-wall region. In order to study the direct relationship between turbulent vortical structures and DR under the control, temporal evolution with initial eddies extracted by the conditional averages for Reynolds-stress-maximizing Q2 events are examined. It is shown that the generation of new vortices is dramatically inhibited with increasing the parameters throughout the flow, and thus fewer vortices are induced under the control. But, when P/h is sufficiently large, the autogeneration process for new vortex is not suppressed over the no-control surface in the near-wall region, thus resulting in increase of the second- and fourth-quadrant Reynolds shear stresses. Although strong amplitude A intensifies near-wall flow properties of turbulence, the increase of the turbulence activity is attributed to generation of counter-clockwise near-wall vortices by the increased vortex transport.

Keywords: Turbulent boundary layer, Direct numerical simulation, Drag reduction, Turbulent structure

Contents

List of Figures····· ii

1. Introduction····· 1

2. Numerical method····· 4

3. Shear-free control····· 6

4. Turbulent statistics····· 12

5. Turbulent structure····· 19

5.1 Quadrant analysis····· 19

5.2 Vortical structures····· 20

5.3 Autogeneration····· 22

6. Summary and conclusions····· 36

REFERENCES····· 39

List of Figures

Figure 2. 1 Schematic of longitudinal control (white) and no-control (black) surfaces of the no- repeatedly arranged in the spanwise direction in turbulent channel flow. The width with the total pitch *P*. *AR* denotes area ratio of control surface to the entire surface. ····· 6

Figure 3. 1 Temporal variation of the skin-friction drag coefficients for manipulated turbulent channel flows by the shear-free control and *v*- and *w*- control schemes. For comparison, data from a fully developed turbulent channel flow with no-control is included.····· 9

Figure 3. 2 Variations of normalized drag as a function of *P/h* and *AR* in turbulent channel for flows: (a) *AR*=0.5 and (b) *P/h*=0.375. Previous DNS data of Park et al. [19] for fully developed channel flows over SHSs using shear-free boundary condition is included comparison.····· 10

Figure 3. 3 Time history of the skin-friction drag coefficients in turbulent channel flows under the SSFC with varying forcing amplitude *A*. Here, *AR*=0.5 and *P/h*=0.375. ····· 10

Figure 3. 4 Variations of normalized drag with increasing amplitude *A* in turbulent channel flows under the SSFC. (a) *AR*=0.5 and (b) *P/h*=0.375.····· 11

Figure 3. 5 Net power saving rates with increasing amplitude *A* under the SSFC. (a) *AR*=0.5 and (b) *P/h*=0.375.····· 11

Figure 4. 1 Mean streamwise velocity gradient profiles normalized by the initial friction by the velocity $u_{\tau o}$. The inset in each figure indicates mean streamwise velocity normalized local friction velocity u_{τ}. The profiles are compared (a) with several control methods with *AR*=0.5, *P/h*=0.375 and *A*=1, (b) with varying *P/h* for *AR*=0.5 and *A*=1, (c) with varying *AR* for *P/h*=0.375 and *A*=1, and (d) with varying *A* for *AR*=0.5 and *P/h*=0.375. Two dashed lines for $U^+=y^+$ and $U^+=2.5\ln y^+ +5.5$ are included in the insets.····· 15

Figure 4. 2 Profiles of turbulent Reynolds stresses with increasing *P/h* for *AR*=0.5 and *A*=1 in the outer coordinates. For *v*- and *w*-controls and shear-free control, *AR*=0.5, *P/h*= 0.375 and *A*=1. The insets are logarithmic plots of the Reynolds stresses normalized by $u_{\tau o}$ to clarify near-wall behavior.····· 16

Figure 4. 3 As the same in figure 4.2, but with increasing *A* for *P/h*=0.375 and *AR*=0.5 under the SSFC.····· 17

Figure 4. 4 Root-mean-square of vorticity fluctuations normalized by $u_{\tau o}^2 / \nu$ with increasing f) *P/h* for fixed *AR*=0.5 and *A*=1 (left column) and with increasing *A* for fixed *P/h*= 0.375 and *AR*=0.5 (right column). (a, b) streamwise, (c, d) wall-normal, and (e, f)

spanwise components. For *v*- and *w*-controls and shear-free control, *P/h*=0.375, *AR*=0.5 and *A*=1. The insets are logarithmic plots in the inner coordinates to clarify near-wall behavior.····· 18

Figure 5. 1 Reynolds shear stress from each quadrant $\langle R_{12} \rangle_{\mathrm{Qi}}^{xz}$ normalized by $u_{\tau o}$ (a, b) with increasing *P/h* for fixed *AR*=0.5 and *A*=1 and (c, d) with increasing *A* for fixed *P/h*=0.375 and *AR*=0.5. The indices i of Qi imply 1, 2, 3 and 4.····· 26

Figure 5. 2 Visualization of vortical structures in turbulent channel flows under the SSFC λ_{ci} is varying *P/h* for *AR*=0.5. (a) no-control flow, (b) *P/h*=0.094, (c) *P/h*=0.188, (d) *P/h* =0.75, (e) *P/h*=1.5 and (f) *P/h*=3. The distance of ticks is 0.5*h*. The contour is normalized by U_c/h and the contour of 17% of the maximum employed to depict the structures. The grey and white colors on the bottom indicate control and no-control surfaces.····· 27

Figure 5. 3 As the same in figure 5.2, but for *P/h*=0.375 and *AR*=0.5 as a function of amplitude *A*. (a) no-control flow, (b) *A*=1.000, (c) *A*=1.008, (d) *A*=1.010, (e) *A*=1.011 and (f) *A*=1.012.····· 28

Figure 5. 4 Inner-scaled (a) vortex stretching term and (b) vortex transport term with increasing *A* for fixed *P/h*=0.375 and *AR*=0.5.····· 29

Figure 5. 5 Linear stochastic estimation of $< u_j'(\boldsymbol{x}') \left| \lambda_{ci}(\boldsymbol{x}) \right. >$ at y_{ref}^+ =30.3. Closed circle and square indicate the clockwise and counter-clockwise rotating vortices respectively. (a) no-control flow, (b,c) control flows: (b) *A*=1.010 and (c) *A*=1.012. (i) no-control surface and (ii) control surface. In (b) and (c), *P/h*=0.375 and *AR*=0.5.····· 29

Figure 5. 6 Distribution of (*u'*,*v'*) at y_{ref}^+ =10. (a) no-control flow and (b, c) control flow for *A*=1.012, *P/h*=0.375 and *AR*=0.5: (b) no-control surface and (c) control surface.····· 30

Figure 5. 7 Probability weighted Reynolds shear stress *u' v'*p.d.f.(*u'*,*v'*) at y_{ref}^+ =30.3. (a) no-control flow, (b) control flow for *P/h*=3, *AR*=0.5 and *A*=1 and (c) control flow for *P/h*=0.375, *AR*=0.5 and *A*=1.012. Here, u_i' is the velocity stochastic component and $\langle \cdot \rangle$ indicates time- and streamwise-averaged quantities.····· 31

Figure 5. 8 The evolution of initial vertical structure extracted by Q2 event vector of strength α=2 at y_{ref}^+ =30.3. Vortices are shown using the isosurfaces of 25% of the maximum swirling strength (λ_{ci}) of the initial eddy: (a) no-control flow and (b-e) control flows: (b) *P/h*=1.5, (c) *P/h*=3, (d) *A*=1.008 and (e) *A*=1.012. (i) and (ii) indicate control and no-control surfaces. In (b) and (c), *AR*=0.5 and *A*=1 and in (d) and (e), *P/h*= 0.375 and *AR*=0.5.····· 32

Figure 5. 9 The evolution of initial vertical structure extracted by Q2 event vector of strength α=3 at y_{ref}^{+} =97.6. Vortices are shown using the isosurfaces of 30% of the maximum swirling strength (λ_{ci}) of the initial eddy. (a) no-control flow and (b-d) control flows: (b) *P/h*=0.047, (c) *P/h*=1.5 and (d) *P/h*=3. (i) and (ii) indicate control and no-control surfaces. For (b-d), *AR*=0.5 and A=1.····· 33

Figure 5. 10 The evolution of initial vertical structure extracted by Q2 event vector of strength α=3 at y_{ref}^{+} =97.6. Vortices are shown using the isosurfaces of 30% of the maximum swirling strength (λ_{ci}) of the initial eddy. (a) no-control flow and (b-d) control flows: (b) *A*=1.000, (c) *A*=1.008 and (d) *A*=1.012. (i) and (ii) indicate control and no-control surfaces. In (b-d), *P/h*=0.375 and *AR*=0.5.····· 34

Figure 5. 11 The volume averaged |-*u'v'*| scaled by its initial value during evolution of the initial structures extracted by Q2 event vector with increasing (a) *P/h* with α=2 at y_{ref}^{+} = 30.3, (b) *A* with α=2 at y_{ref}^{+} =30.3, (c) *P/h* with α=3 at y_{ref}^{+} =97.6 and (d) *A* with α=3 at y_{ref}^{+} =97.6. ····· 35

Figure 6. 1 The evolution of initial vertical structure extracted by Q2 event vector of strength α=2 and 3 at y_{ref}^{+} =30.3 (a, b) and 97.6 (c, d). Structures indicate iso-surfaces of 25 % and 30% of the maximum swirling strength λ_{ci} respectively: (a, c) SSFC and (b, d) shear-free control. (i) and (ii) indicate control and no-control surfaces. In (a-d), *P/h*= 1.5, *AR*=0.5 and *A*=1.····· 38

1. Introduction

Over several decades, significant efforts have been devoted to reduction of skin-friction drag in wall-bounded turbulent flows due to limited natural resources and environmental deterioration [1]. Because decreasing the drag also induces reduction of structural vibrations, noise and surface heat transfer generated by turbulent flows [2], it is desirable to develop effective and reliable flow control strategies for drag reduction (DR) in many engineering applications.

The control methods for DR can be largely classified into active and passive controls. The active control has been also categorized into closed-loop control [3, 4, 5, 6] and open-loop control [7, 8, 9]. As a closed-loop feedback flow control scheme, Choi et al. [3] devised opposition control method (OCM) for the wall-normal and spanwise velocity components to suppress energetic near-wall streamwise vortices associated with high skin-friction drag, and they reported DR up to 20%-25% at y_d^+=10, where y_d^+ is sensing location from the wall and the superscript + refers to a non-dimensional quantity normalized by the local friction velocity and the viscous length scale. A subsequent DNS study by Chung & Sung [10] with the OCM showed that situating detection plan at y_d^+=15 results in a higher efficient DR than that at y_d^+=10. Furthermore, Chung & Talha [11] found that an optimal amplitude *A* for blowing and suction at the wall for better efficiency depends on wall-normal location for detection plane through $5 \leq y_d^+ \leq 30$. The optimal *A* of detection plane located at y_d^+<15 was *A*=1, whereas in a case of y_d^+>15, the optimal *A* was less than 1. Kasagi et al. [1] showed that the net energy saving rate for the OCM with the wall-normal velocity is approximately 17%.

However, even though the OCM provides a high DR rate, it has been reported two significant shortcomings: *i*) it requires velocity information inside the flow domain, and thus the sensor within the flow could disturb the upcoming flow, and *ii*) many sensors and actuators are needed to control the flow for the rapid reversal of blowing and suction through the entire domain, making hardware system complicated with overload [1]. To avoid measurement of the velocity inside the flow, Koumoutsakos [12] proposed a control method using manipulation of wall vorticity flux to provide the strength of the unsteady mass/blowing.

In addition to the OCM method, recent advances in our understanding of wall turbulence have enabled further progress towards the development of effective closed-loop control schemes. These include suboptimal control [4, 5], control using spatial relationship between measurable wall quantities and the near-wall streamwise vortices [6] and linear mechanism control [2].

For open-loop flow control strategies, a wide variety of different types have been developed over the years including spanwise wall oscillation [13], streamwise/spanwise traveling wave control [7, 9] and steady/unsteady blowing and suction [8]. Because methods described above do not require any sensor in order to determine actuator operation, it could be a better way to overcome the drawbacks of

the closed-loop controls. Using the spanwise wall oscillation, Quadrio & Ricco [13] found a maximum DR of 44.7% and a maximum net energy saving of 7.3%. Several studies based on streamwise/spanwise traveling wave control showed that a maximum DR is about 57%, and a maximum net energy saving rate is 28% with consideration of the power consumption [7, 9]. Although the open-loop flow control methods provide a highly sufficient DR rate, it needs a rather high power input to induce the controlled motions of turbulent flows.

For passive control of turbulent flows for DR, various techniques using addition of polymers [14], riblets [15] and compliant walls [16] have been proposed so far. In particular, superhydrophobic surfaces (SHSs) constructed by a combination of micro- and/or nano-scale surface features and a hydrophobicity by chemical coating have been recently received much attention, because slip velocity created by shear-free condition on air-water interface over hydrophobic surfaces results in significant DR [17- 21]. Two different models have been widely adopted in DNS studies to describe the SHSs on the wall. Philip [22] modeled the SHS as an alternating boundary condition between no-slip and slip using the Navier slip boundary condition ($u_s=l_s(\partial u/\partial y)_0$, $w_s=l_w(\partial w/\partial y)_0$), where ($u_s$, w_s) are the slip velocities in the streamwise and spanwise directions and (l_s, l_w) are the corresponding effective slip lengths, for solid-fluid interfaces on microscopic scale. In a DNS study of a turbulent channel flow using the Navier slip model, Min & Kim [17] reported that when the slip boundary condition is given through the whole wall, there is a reduction of turbulent drag up to 29% depending on the slip length and shear-free condition. However, when a slip boundary condition is only given in the spanwise direction, the drag was enhanced in their study. It should be noted that a very recent DNS study of Jung et al. [23] examined effects of air layer over SHSs on the slip behavior at the interface by considering two different flow types inside the air layer and showed that the air-water interface generates an anisotropic slip, and the streamwise slip length is larger than the spanwise one.

Compared to boundary condition with a spatially uniform slip length prescribed, the SHSs can be also modeled by alternating no-slip and shear-free boundary conditions, $(\partial u/\partial y)_0=(\partial w/\partial y)_0=0$, on air-water interface [18, 19, 24, 25]. In this setup, a homogeneous slip length is not given *a priori*. However, it is noted that the shear-free condition at the interface could not be valid in real application. Using the shear-free boundary condition, recent studies for turbulent channel flows with longitudinal SHSs have shown that two parameters (e.g., width fraction of the SHS to no-slip wall and a total pitch length) are important to characterize drag reducing performance of the surfaces: *i*) As the fraction of the SHSs increases, the drag continuously decreases, and *ii*) as the spanwise pitch of the SHSs increases, the DR rate gradually converges to a certain value [18, 19]. In addition, it has been shown that the DR rate in turbulent flows with SHSs strongly depends on pattern types of the SHSs on the wall (e.g., longitudinal, transverse and post), and maximum DR up to 80% is found on a wall comprised of longitudinal SHSs [18, 20].

Although there have been reported high rate of DR in turbulent flows over SHSs, the solid-liquid interface in practice is not self-maintained by nature unless gas bubble is artificially supplied into a cavity by extra energy. Because characteristics of air pockets is influenced by width of the solid-liquid interface, pressure fluctuations, impact velocities, vibrations, contamination effect and two-phase thermodynamic interactions and so on [26, 27], it is nearly impossible to sustain the solid-liquid interface in reality as designed as an ideal circumstances for SHSs, e.g. no air loss and flat solid-liquid interface [28, 29]. In addition, because air loss within a plastron by diffusion of trapped air could trigger collapse of the solid-liquid interface, it could lead to change from Cassie-Baxter state to Wenzel state, resulting in significant drag increase by surface roughness effect. The technical difficulties with high expense for maintenance of ideal solid-liquid interface make it difficult to utilize the SHSs in real engineering application for DR, in particular in a high Reynolds number turbulent flow.

Despite some difficulties in constructing an idealized solid-liquid interface in reality, numerical scheme (e.g. shear-free condition at the wall) in DNS studies for modeling SHSs is highly attractive due to induction of significant DR. To directly utilize the idea on an active flow control concept aiming at DR, in the present study, we perform a DNS study for fully developed turbulent channel flows. Because the shear-free condition at the wall provides two obvious advantages compared to the OCM that it requires only velocity information at the wall and achieves a large DR rate even over a limited area, an active flow control using the shear-free condition at the wall could be a more practical and efficient method in application as a closed-loop control scheme. The actuating velocity at the wall can be easily obtained from shear stress sensors in experiment that have been significantly developed by MEMS fabrication technologies recently [30].

To show promise of the current method for DR in turbulent flow with less actuators and sensors at the wall, we assume that the actuators and sensors are arranged in an alternative longitudinal pattern (e.g., no-control and control surfaces) through the wall region, similar to previous studies for turbulent flows with SHSs. Many DNSs of turbulent channel flows with symmetric walls are performed to examine flow physics related to the shear-free control at the wall. The DR rate, net power saving rate and associated turbulent statistics are examined and compared with results from the OCM under the same geometric configuration. In addition, the influence of amplitude parameter to impose the strength of actuating velocity at the wall is studied in order to enhance DR. The modification of turbulent structures are documented through quadrant analysis, instantaneous view of vortical structures, analysis of vortex stretching and transport terms and conditionally averaged flow fields. Finally, single eddy simulations are conducted to provide a clear picture for mechanism of DR in the presence of the SSFC in the near-wall and outer regions.

2. Numerical method

For an incompressible flow, the Navier-Stokes and the continuity equations are

$$\frac{\partial u_i}{\partial t}+\frac{\partial u_i u_j}{\partial x_j} = -\frac{\partial p}{\partial x_i}+\frac{1}{Re}\frac{\partial^2 u_i}{\partial x_j \partial x_j}$$

$$\frac{\partial u_i}{\partial x_i} = 0$$

where x_i denotes the Cartesian coordinates and u_i represents the corresponding velocity components. All variables are non-dimensionalized by the channel half-height (h) and the laminar centerline velocity (U_c). The equations are integrated over time using the fractional step method along with the implicit velocity decoupling procedure [31]. Based on a block LU decomposition, both velocity-pressure decoupling and the decoupling of the intermediate velocity components are achieved in conjunction with the approximate factorization. The terms are initially discretized in time using the Crank-Nicholson method, and then the coupled velocity components are solved without iteration. All terms are resolved using a second-order central difference scheme in space with a staggered mesh. To drive flow with a fixed mass flow rate, the mean pressure gradient is adjusted.

Notation adopted is that x, y, and z denote the streamwise, wall-normal, and spanwise coordinates, respectively, and that u, v, and w denote the corresponding velocity components. The computational domain (L_x x L_y x L_z) is $6h$ x $2h$ x $3h$, which is similar to previous studies with SHSs [19], and the corresponding mesh size are 192 x 129 x 128, resulting in grid resolutions of Δx^+=5.5, $\Delta y_{min}{}^+$=0.29, and Δz^+=4.1, respectively. Non-uniform grid distributions are applied in the wall-normal direction using the hyperbolic tangent function and a uniform grid distribution in both the streamwise and spanwise directions. Periodic boundary conditions are used along the streamwise and spanwise directions. On the bottom and top walls, the boundary condition is given to control the flow using streamwise $\left(\frac{\partial u}{\partial y}\right)_w = 0$ and spanwise $\left(\frac{\partial w}{\partial y}\right)_w = 0$ velocity shear-free condition in a limited area, and the other area is considered using a no-slip condition.

An initial velocity field for the flow control is provided using a DNS data for a fully developed turbulent channel flow with regular no-slip condition at the wall. The Reynolds number is $Re_{c,o}$(=$U_c h/\nu$)=4200, and the corresponding Kármán number is $Re_{\tau,o}$(= $u_{\tau,o}h/\nu$)=180 based on the friction velocity on a regular no-slip channel wall ($u_{\tau,o}$), where ν is the kinematic viscosity of the fluid. The subscript ‘o’ indicates value on a regular channel wall.

In the present study, the channel flow is assumed to be actively controlled on limited longitudinal surfaces for simplicity (figure 2.1). The control surface of width P-W (white) is repeatedly arranged in the spanwise direction with no-control surface of width W (black), and the control is achieved on top and bottom walls. In addition to the longitudinal array, it is possible to consider various patterns for

limited control regions, for example, transverse and post type regions. However, although not shown here, the reduction of drag is confirmed to be highly efficient in the longitudinal array, consistent with previous study of Rastegari & Akhavan [20] in turbulent channel flow with SHSs. The velocity shear-free condition for flow control at each instant is achieved using velocity component obtained from instantaneous wall shear stress at previous time step. Although the flow convects along the streamwise direction during the time interval Δt, skin-friction reduction is found to be little affected due to small value of Δt. Many simulations are performed with varying the pitch P/h and the area ratio AR between no-control and control surfaces for the purpose of high DR using the same initial velocity field.

Because the SSFC is applied through a limited area on the entire wall, it is natural to anticipate spatial variation of flow characteristics statistically, requiring phase-averaging in space. For phase-averaging in the spanwise direction, a spanwise phase with respect to the periodic surface at the wall is

$$\phi_z \equiv 2\pi\left(\frac{z}{P} \bmod 1\right),$$

and a phase-averaging operator leading to a triple decomposition of the velocity as suggested by Reynolds & Hussain [32] is decomposed as,

$$\begin{aligned} u_i(\boldsymbol{x},t) &= \underbrace{\langle u_i(\boldsymbol{x},t)\rangle^{xz} + \tilde{u}_i(y,\phi_z)}_{\langle u_i\rangle} + u_i'(\boldsymbol{x},t) \\ &= \langle u_i\rangle(y,\phi_z) + u_i'(\boldsymbol{x},t), \end{aligned} \tag{2.1}$$

where u_i' is the velocity stochastic component and u_i is the instantaneous velocity variable. $\langle\cdot\rangle$ indicates time- and streamwise-averaging (e.g., phase-averaging) and $\langle\cdot\rangle^{xz}$ depicts space-averaging in the horizontal direction (e.g., $U_i = \langle u_i\rangle^{xz}$). $\langle\cdot\rangle^{xz}$ can be obtained from phase-averaging over no-control and control surfaces $\langle\cdot\rangle^{ns}$ and $\langle\cdot\rangle^{cs}$, respectively, and for AR=0.5,

$$\langle u_i\rangle^{xz} = \frac{1}{2}\left(\langle u_i\rangle^{ns}(y) + \langle u_i\rangle^{cs}(y)\right). \tag{2.2}$$

In addition, the phase-averaged Reynolds stresses over no-control and control surfaces are decomposed as

$$\begin{aligned} \langle R_{ij}\rangle^{ns}(y) &= \langle u_i(\boldsymbol{x},t)u_j(\boldsymbol{x},t)\rangle^{ns} - \langle u_i(\boldsymbol{x},t)\rangle^{ns}\langle u_j(\boldsymbol{x},t)\rangle^{ns} \text{ and} \\ \langle R_{ij}\rangle^{cs}(y) &= \langle u_i(\boldsymbol{x},t)u_j(\boldsymbol{x},t)\rangle^{cs} - \langle u_i(\boldsymbol{x},t)\rangle^{cs}\langle u_j(\boldsymbol{x},t)\rangle^{cs}. \end{aligned}$$

Then, the plane-averaged Reynolds stresses for AR=0.5 are as follows,

$$\langle R_{ij}\rangle^{xz} = \frac{1}{2}\left(\langle R_{ij}\rangle^{ns}(y) + \langle R_{ij}\rangle^{cs}(y)\right). \tag{2.3}$$

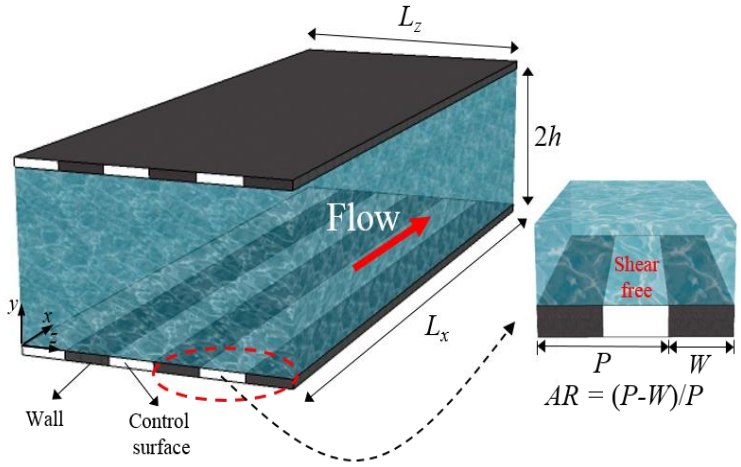

Figure 2.1 Schematic of longitudinal control (white) and no-control (black) surfaces repeatedly arranged in the spanwise direction in turbulent channel flow. The width of the no-control wall is denoted by *W* and that of the control surface is expressed by *P-W* with the total pitch *P*. *AR* denotes area ratio of control surface to the entire surface.

3. Shear-free control

To assure the effectiveness of the shear-free control for skin-friction reduction in turbulent flow, variation of the skin-friction drag coefficients in fully developed turbulent channel flows subjected to two different shear-free controls, e.g. shear-free control in the streamwise direction and shear-free control both in the streamwise and spanwise directions is examined in figure 3.1. Although not shown here, the mean pressure gradient necessary to drive a constant mass flow rate for the no-control and control channel flows is changed in time similarly to that of the skin-friction drag [3]. Furthermore, results of the shear-free controls are compared with those of *v*- and *w*-control methods when the controls are applied to the entire wall (*AR*=1) and only a partial wall is manipulated (*AR*=0.5 and *P/h*=0.375). Consistent with the previous study of Choi et al. [3], skin-friction reduction for the out-of phase *v*- and *w*-control schemes through the whole wall layer is achieved about 20~25% at y_d^+=10 in a mean sense, and the *w*-control (~ 25%) is more effective than that of the *v*-control (~ 20%). The manipulated channel flow with the shear-free controls through the entire wall (*AR*=1) in figure 3.1 shows that the skin-friction drag approaches to zero due to no velocity shear at the wall, indicating that the shear-free controls are the ideal active control schemes for highly sufficient skin-friction DR without any disturbance within the flow.

Because many actuators and sensors for the control at the wall both make a system overload and

require high expense for establishment and maintenance of the system [1], it is necessary to control turbulent flow in a limited area. In figure 3.1, as a representative, we choose AR=0.5 and P/h=0.375 for the longitudinal array. Under the current configuration, the v- and w-controls induce skin-friction reduction of about 10%, whereas it is 32% for the shear-free control both in the streamwise and spanwise direction and 38% for the shear-free control in the streamwise direction. The slight increase of the skin-friction drag by the shear-free control through the horizontal plane is due to a negative influence of the spanwise shear-free control on DR, as reported in turbulent channel flow [17, 33]. Because the objective of present study is to investigate active shear-free control strategy for the purpose of high DR, we only apply streamwise shear-free control (SSFC) to channel flows in the following section. This choice also provides a lot of benefit in real application for flow control, because *i*) measuring the spanwise wall-shear stress is not easy at the wall due to diminishing scales of turbulence toward the wall [34] and *ii*) simultaneous measurement of the two transverse velocities requires more complex devices in practical implementation.

In order to show effect of P/h and AR on skin-friction drag, we calculate many simulations of turbulent channel flows under the SSFC using the same initial velocity condition. The results are indicated in figure 3.2 with those of the v- and w-control methods. Here, the drag is calculated by the plane-averaged skin-friction coefficient compared to a value obtained from a no-control fully developed channel flow (Drag=C_f/C_{fo}). Direct comparison of our data with previous DNS data of Park et al. [19] for fully developed channel flows over SHSs shows an excellent agreement, showing accuracy and reliability of the present numerical simulations. In figure 3.2(a), with increasing P/h for a fixed AR=0.5, the skin-friction drag of the channel flows with the v- and w-controls (triangles) have the maximum reduction of 15% at small P/h, and it approaches to a higher steady value rapidly (~10%). The drag under the SSFC (circle) is largely smaller than the v- and w-controls, and it continuously decreases, reaching to a minimum turbulent drag with approximately 45% magnitude. The SSFC of the turbulent channel flows results in slightly larger DR (3~6%) than the shear-free control (square) throughout all P/h, and a similar trend is shown in variation of the normalized drag with varying AR at a fixed P/h in figure 3.2(b), regardless of AR. Although the drag significantly decreases with increasing AR, large value of AR needs many sensors and actuators at the wall. Contrary to the behavior in figure 3.2(a), the v- and w-controls with varying AR indicate an almost linear decrease of the drag. For small AR, it is indicated negligible difference of the drag between the v- and w-controls, but the w-control results in higher DR (~ 5%) than that of v-control for large AR (>0.7), similar to previous observation of Choi et al. [3].

Although the SSFC results in the significant DR, compared to the opposition control and shear-free control, the maximum turbulent DR possible is about 55%, when the turbulent channel flows are controlled over half of the entire wall (AR=0.5 and P/h=3). To further increase skin-friction DR, we introduce an amplitude parameter (A) to describe the strength of wall streamwise velocity at time t,

$$u(x,0,z;t) = Au(x,\Delta y,z;t-\Delta t),$$

where y=0 indicates the wall and $y=\Delta y$ indicates the nearest wall-normal grid point to the wall. Wall streamwise velocity at t for the control is acquired from the previous time instant $t-\Delta t$. In figures 3.1 and 3.2, A=1 is employed, and it induces streamwise shear-free condition $\partial u/\partial y$=0 at the wall. If A is larger than 1, $\partial u/\partial y$ is less than zero, i.e. negative wall-shear stress at the wall, decreasing total skin-friction drag in the flow.

Temporal variation of skin-friction coefficients under the SSFC with varying forcing amplitude A is shown in figure 3.3. As A increases with interval of 0.002 at fixed AR=0.5 and P/h=0.375, the skin-friction drag continuously decreases, and a maximum turbulent DR is found at A=1.012 (only 1.2% increase compared to A=1) with approximately 87%. Although not shown here, further increasing A leads to more DR, for example, 99.4% DR at A=1.013, and the drag becomes negative for A>1.013. In figure 3.4, variation of normalized drag as a function of A is studied at fixed AR and P/h. As expected, for large P/h (figure 3.4a) and AR (figure 3.4b), the normalized drag rapidly decreases as amplitude A increases, and thus applying a 0.5~0.6% larger control input for P/h=1.5 and 3 with AR=0.5 results in almost 90% DR in figure 3.4(a). Although influence of A is negligible for small P/h and AR with a slow decreasing rate (circle symbols), the normalized drag for intermediate values P/h and AR (square symbols) shows two different decreasing slopes of lines with increasing A, showing that the drag under the SSFC is sensitive to forcing amplitude A. In the present study, we consider amplitude A larger than 1, because an amplitude A less than 1 leads to less DR than those of A=1 in turbulent channel flow under the SSFC.

Although the SSFC of turbulent channel flows results in dramatic DR, it is not clear how much the net energy saving rate is achieved. The SSFC's actuator power is calculated based on suggestion of Quadrio et al. [9],

$$P(\%) = \frac{100}{\left(dU/dy\right)_w U_b} \frac{1}{L_x L_z T} \int_0^{L_x}\int_0^{L_z}\int_0^{T} u_w \left.\frac{\partial u}{\partial y}\right|_w dtdzdx \qquad (3.1)$$

where $(dU/dy)_w$ is the wall-normal gradient of the mean streamwise velocity at the wall and u_w indicates the streamwise velocity at the wall. Then, the net energy saving rate is calculated by

$$P_{net}(\%) = DR(\%) - P(\%) \qquad (3.2)$$

i.e. the efficiency of the SSFC is given as amount of external energy used to input velocities. Figure 3.5 shows the net energy saving rates with varying P/h and AR as a function of amplitude A. With increasing P/h and AR, the net energy saving rate for small A increases. For large A, however, the net energy saving rate rapidly decreases especially for large P/h and AR. The maximum net energy saving rates with fixed AR and P/h in figures 3.5(a) and (b) are observed at the largest P/h (~56.8%) and AR (~83.8%) for A=1.002 and 1.001 respectively. These observations in figures 3.4 and 3.5 suggest that although the use of the forcing amplitude increases the reduction of the skin-friction drag rapidly, it

reversely deteriorates the net energy efficiency for some cases (see square and lower triangular symbols), compared to A=1 case. However, it should be mentioned that for small A (<1.004), increasing the amplitude leads to slight increase (or almost constant) of the net energy saving rates with significant DR in particular for large P/h and AR. In addition, positive saving rates in figure 3.5, except for large A with large P/h and AR, imply potential for large turbulent skin-friction DR with high net energy saving rate.

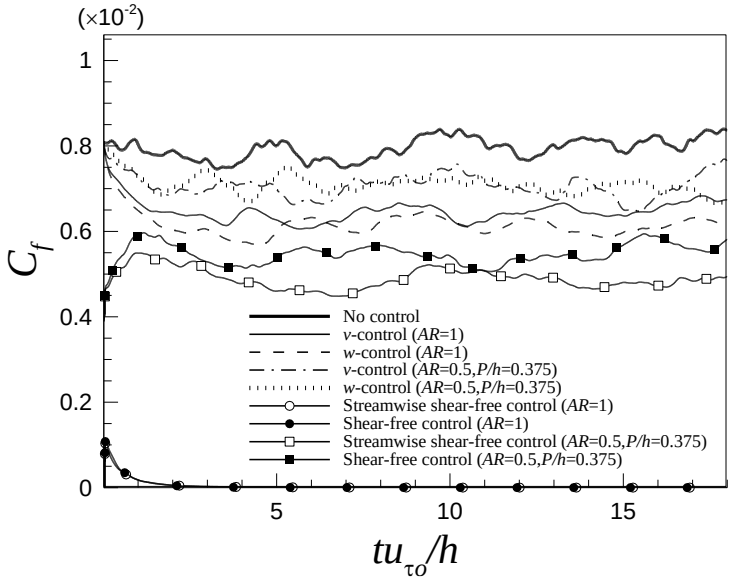

Figure 3. 1 Temporal variation of the skin-friction drag coefficients for manipulated turbulent channel flows by the shear-free control and *v*- and *w*- control schemes. For comparison, data from a fully developed turbulent channel flow with no-control is included.

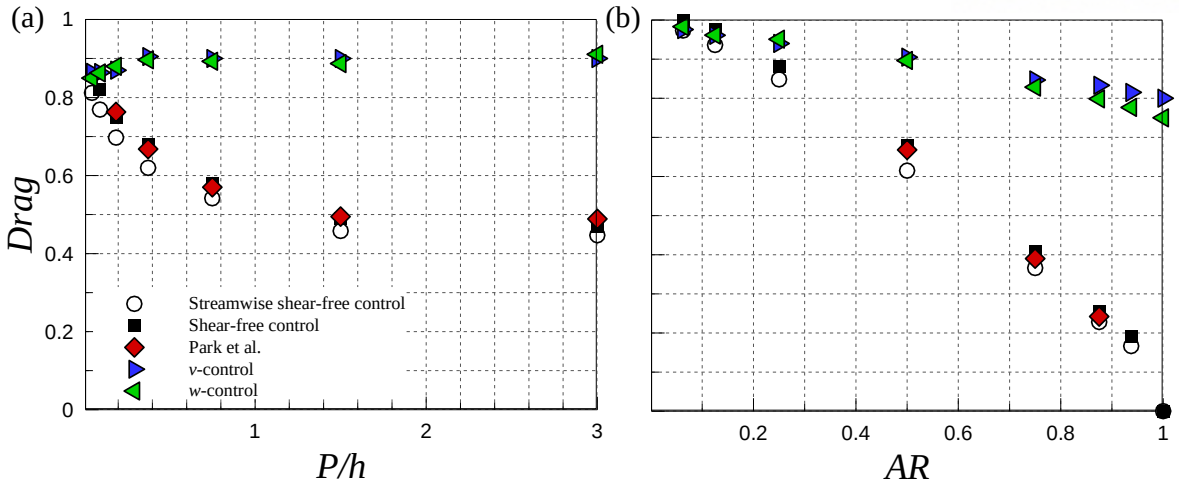

Figure 3. 2 Variations of normalized drag as a function of *P/h* and *AR* in turbulent channel flows: (a) *AR*=0.5 and (b) *P/h*=0.375. Previous DNS data of Park et al. [19] for fully developed channel flows over SHSs using shear-free boundary condition is included for comparison.

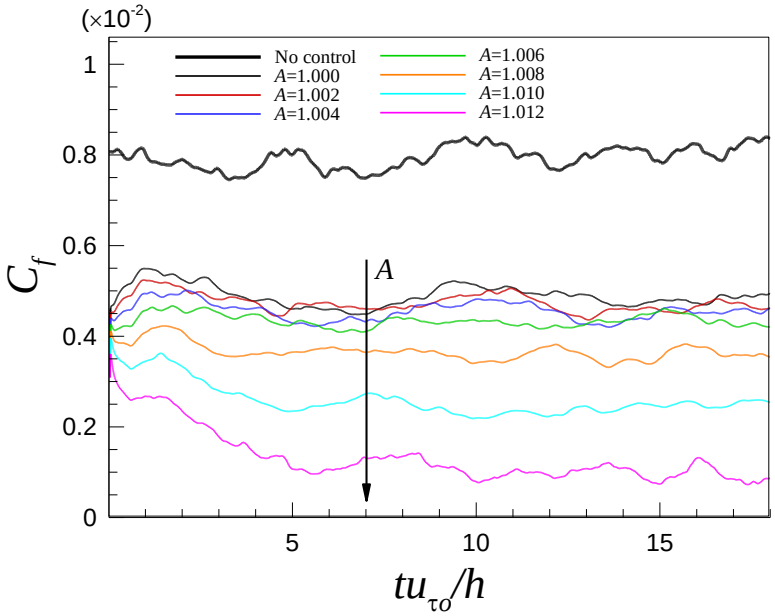

Figure 3. 3 Time history of the skin-friction drag coefficients in turbulent channel flows under the SSFC with varying forcing amplitude *A*. Here, *AR*=0.5 and *P/h*=0.375.

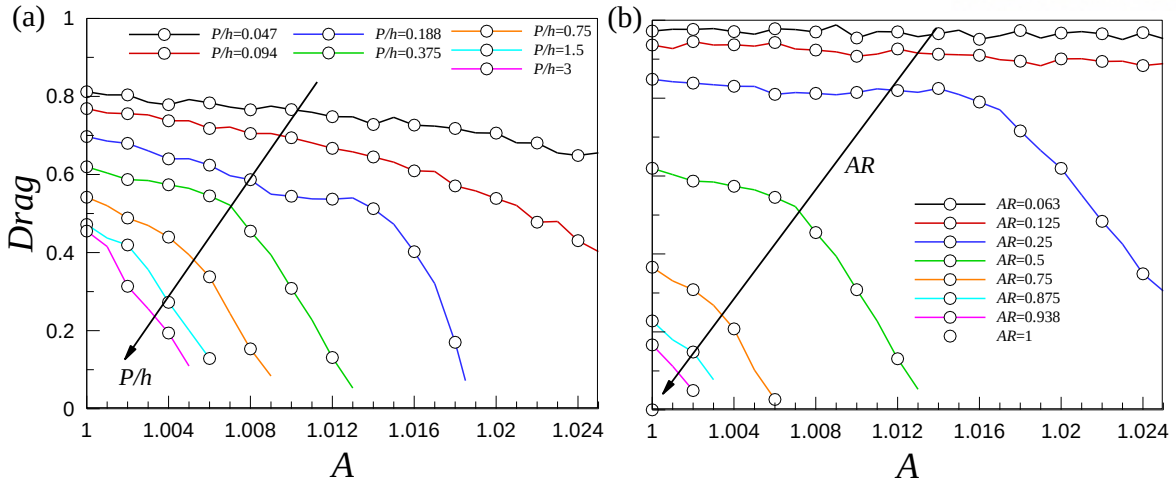

Figure 3. 4 Variations of normalized drag with increasing amplitude *A* in turbulent channel flows under the SSFC. (a) *AR*=0.5 and (b) *P/h*=0.375.

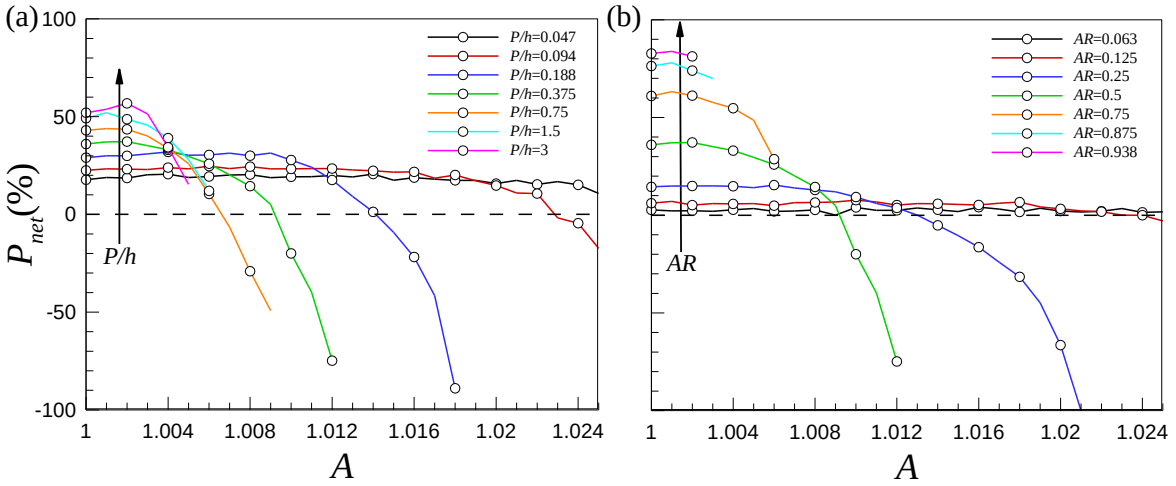

Figure 3. 5 Net power saving rates with increasing amplitude *A* under the SSFC. (a) *AR*=0.5 and (b) *P/h*=0.375.

4. Turbulent statistics

In this section, turbulent statistics of the channel flows under the SSFC are analyzed to show effect of the control scheme. Furthermore, results are compared with those of *v*- and *w*-controls and shear-free control with varying *P/h*, *AR* and *A* respectively. To carry out analysis to a normalizing variable, all velocity components are primarily normalized by $u_{\tau o}$, and length scale is normalized by viscous length scale $\nu/u_{\tau o}$ or outer length scale *h*. In addition, some discussion with statistics normalized by local friction velocity is given. The first and second-order statistics described in the following are performed based on the definitions of (2.2) and (2.3), and definition for the others are indicated in the corresponding section. Because variation of the turbulent statistics with varying *P/h* and *AR* is very similar, we show only results with varying *P/h*.

The mean velocity gradient profiles scaled by the initial friction velocity ($u_{\tau o}$) are indicated in figure 4.1(a) under various control schemes for fixed *AR*=0.5, *P/h*=0.375 and *A*=1. In addition, the insets in the figures show mean velocity profiles scaled by local friction velocity (u_τ). It is evident distortion of mean velocities by the controls compared to no-control turbulent channel flow (bold solid line). The mean streamwise velocity shear near the wall is decreased when flows are controlled. In particular, the SSFC and shear-free control result in large reduction of the shear than the *v*- and *w*-controls, showing larger turbulent skin-friction DR in the SSFC and shear-free control under the same configuration parameters. The slope of the log-law in the mean velocity profiles are not affected by the control effect and as there occurs more DR, the log law is more largely shifted upward, consistent with previous drag-reducing flows such as riblets [15] and polymers [14]. The near-wall velocities under the SSFC and shear-free control are shifted upward due to the input velocity. As *P/h*, *AR* and *A* increase in figures 4.1(b-d), it is evident that the mean velocity gradient continuously decreases in the near-wall region (hence, larger DR). Although not shown here, normalization of the mean velocity gradients with u_τ indicates a thickening of the viscous sublayer with increasing *P/h*, *AR* and *A*, and turbulence motions in the flows under the controls are more suppressed. Furthermore, because the mass flow rate is constant, the mean velocities normalized by $u_{\tau o}$ decrease in the core region as *P/h*, *AR* and *A* increase.

The distribution of the Reynolds stresses scaled by $u_{\tau o}$ is present in figure 4.2, as the SSFC is induced as *P/h* increases for fixed *AR*=0.5 and *A*=1. In addition, results for *v*- and *w*-controls and shear-free control for fixed *AR*=0.5, *P/h*=0.375 and *A*=1 are indicated for comparison. It is evident that all the Reynolds stresses far from the wall are increasingly reduced under the SSFC as *P/h* increases, compared to those in the no-control flows (bold solid line). However, in the very near-wall region, $y^+<5$, (see the small figures), the streamwise normal stress is enhanced as *P/h* increases because of streamwise velocity input. For the wall-normal and spanwise turbulent stresses and Reynolds shear stress, magnitudes in range of $y/h<0.2\sim0.5$ are continuously decreased up to *P/h*=1.5,

and they are increased for *P/h*=3. It should be noted that the largest reduction of the turbulent Reynolds stresses throughout the outer layer are shown for *P/h*=3, hence resulting in the largest DR for *P/h*=3 (figure 3.2a). Direct comparison of the statistics with the *v*- and *w*-controls and shear-free control for *AR*=0.5, *P/h*=0.375 and *A*=1 displays (see symbols) that magnitudes of the normal Reynolds stresses in the very near-wall region are strongly influenced by their control input. The wall-normal and spanwise Reynolds stresses near the wall are larger for the *v*- and *w*-controls respectively. For the shear-free control, because the streamwise and spanwise velocity shears at the wall are simultaneously controlled, the streamwise and spanwise components of the Reynolds stresses are amplified near the wall. In figure 4.2(c), it indicate that the spanwise normal stress with the *w*-control has larger value than that of the shear-free control near the wall. This is because of that the spanwise velocity input for the *w*-control at the wall is larger due to the higher sensing location at y_d^+=10. On the other hand, the Reynolds shear stress for the same *P/h*, *AR* and *A* is little affected by the control input near the wall, and decrease of the Reynolds shear stress is proportional to rate of DR.

Figure 4.3 indicates the Reynolds stresses profiles scaled by $u_{\tau o}$ as a wall amplitude parameter *A* for the SSFC is varied for fixed *P/h*=0.375 and *AR*=0.5. Far from the wall, continuous decrease of all the statistics is clear as *A* increases, similar to the variation of DR under the SSFC (figure 3.4). In the logarithmic plots with the inner coordinates, the streamwise normal Reynolds stress near the wall (y^+<10) increases as *A* increases, consistent with those as *P/h* increases in figure 4.2(a). The wall-normal and spanwise normal stresses near the wall (y^+<40) are almost similar in the range of *A*=1.000~1.007, whereas they are decreased for *A*=1.008~1.010 because of larger DR with increasing *A*. Further increase of *A* (1.011≤*A*≤1.013) results in significantly larger wall-normal and spanwise Reynolds stresses in the near-wall region, compared to those of the manipulated flow with *A*=1.010 and the unmanipulated flow. The increase of the statistics is closely associated with near-wall vortex generation in self-sustained process as discussed later. For the Reynolds shear stresses in figure 4.3(d), the magnitudes near the wall are almost similar in the range of *A*=1.000~1.007. With increasing *A* (1.008≤*A*≤1.013), the Reynolds shear stresses are gradually decreased and finally become negative with a minimum at y^+~25 for *A*=1.011~1.013. The decrease of the Reynolds shear stress for *A*≥1.008 is related with dramatic decrease of DR in figure 3.4(a) (closed square symbol), because the skin-friction drag is proportional to the weighted Reynolds shear stress distribution [35].

The profile of the root-mean-square vorticity fluctuations scaled by $u_{\tau o}^2/\nu$ is indicated in figure 4.4 as *P/h* increases for fixed *AR*=0.5 and *A*=1 (left column) and with varying *A* for fixed *P/h*=0.375 and *AR*=0.5 (right column). The vorticity fluctuations are examined based on definition of $\langle \omega_i' \rangle^{xz} = \sqrt{\frac{1}{2}\left(\langle (\omega_i')^2 \rangle^{ns} + \langle (\omega_i')^2 \rangle^{cs} \right)}$, where ω_i' is vorticity fluctuating component in Cartesian coordinates. The variation of the vorticity fluctuations far from the wall is similar to that of the

previous Reynolds stress profiles in which the magnitudes are continuously decreased as P/h and A increase, resulting in the largest DR at maximum P/h and A. Furthermore, the streamwise vorticity fluctuations as P/h and A increase in the near-wall region are varied similarly to the wall-normal and spanwise normal stresses. However, the wall-normal vorticity fluctuations with increasing P/h in figures 4.4(c) exhibit that the quantities are continuously decreased with a maximum at around P/h=0.094~0.188 near the wall, because the increase of P/h leads to reduction of $\partial u/\partial z$ which is a dominant contributor to the wall-normal vorticity. It should be noted that for sufficiently small P/h such as P/h=0.047, the magnitude of the spanwise gradient of the streamwise velocity is comparable with that of the no-control channel flow because of little effect of the input velocity on the velocity shear. For the spanwise vorticity fluctuations as P/h increase in figure 4.4(e), all of the data are scattered with no clear dependency on P/h near the wall. In figures 4.4(d) and (f), the wall-normal and spanwise vorticity fluctuations with increasing A are continuously increased in the near-wall region (y^+<15), contrary to the Reynolds stress profiles as A increase in figure 4.3. This is expected because the increase of the amplitude A induces large velocity gradients $\partial u/\partial z$ and $\partial u/\partial y$ than A=1 case.

Comparison of the vorticity fluctuations with those of the v- and w-controls and shear-free control for fixed AR=0.5, P/h=0.375 and A=1 (left column) indicates that the w-control significantly increases the streamwise vorticity fluctuations near the wall. However, the v-control and shear-free control weaken the ones than that of the unmanipulated flow. Because the shear-free control leads to $\partial w/\partial y$=0 at the wall which is a dominant contributor to the streamwise component of the vorticity, it directly decreases streamwise vorticity fluctuations. However, because the SSFC is not related with generation of the streamwise vorticity, decomposed as $\partial w/\partial y$ and $\partial v/\partial z$, it is reasonable to infer that the reduction of the streamwise vorticity fluctuations by the SSFC is probably because of weakening effect of streamwise vortex responsible for generation of the vorticity. The wall-normal vorticity fluctuations in figure 4.4(c) show larger values for the shear-free control and SSFC than those for the v- and w-controls due to large $\partial u/\partial z$ near the boundary between the no-control and control surfaces. The more strict flow control at the wall by the shear-free condition than that of the SSFC creates a larger streamwise velocity shear near the wall, leading to larger wall-normal and spanwise vorticity fluctuations under the shear-free control.

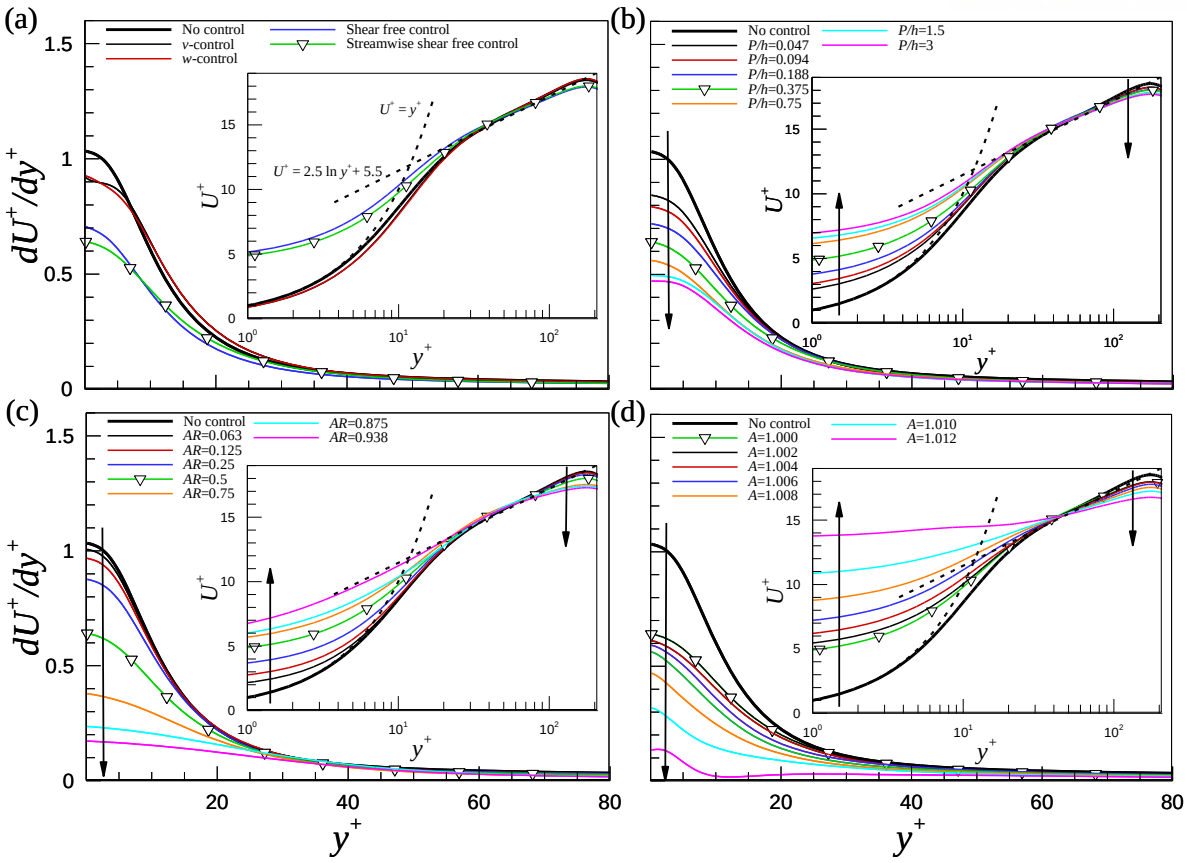

Figure 4. 1 Mean streamwise velocity gradient profiles normalized by the initial friction velocity $u_{\tau o}$. The inset in each figure indicates mean streamwise velocity normalized by the local friction velocity u_τ. The profiles are compared (a) with several control methods with *AR*=0.5, *P/h*=0.375 and *A*=1, (b) with varying *P/h* for *AR*=0.5 and *A*=1, (c) with varying *AR* for *P/h*=0.375 and *A*=1, and (d) with varying *A* for *AR*=0.5 and *P/h*=0.375. Two dashed lines for $U^+=y^+$ and $U^+=2.5\ln y^+ +5.5$ are included in the insets.

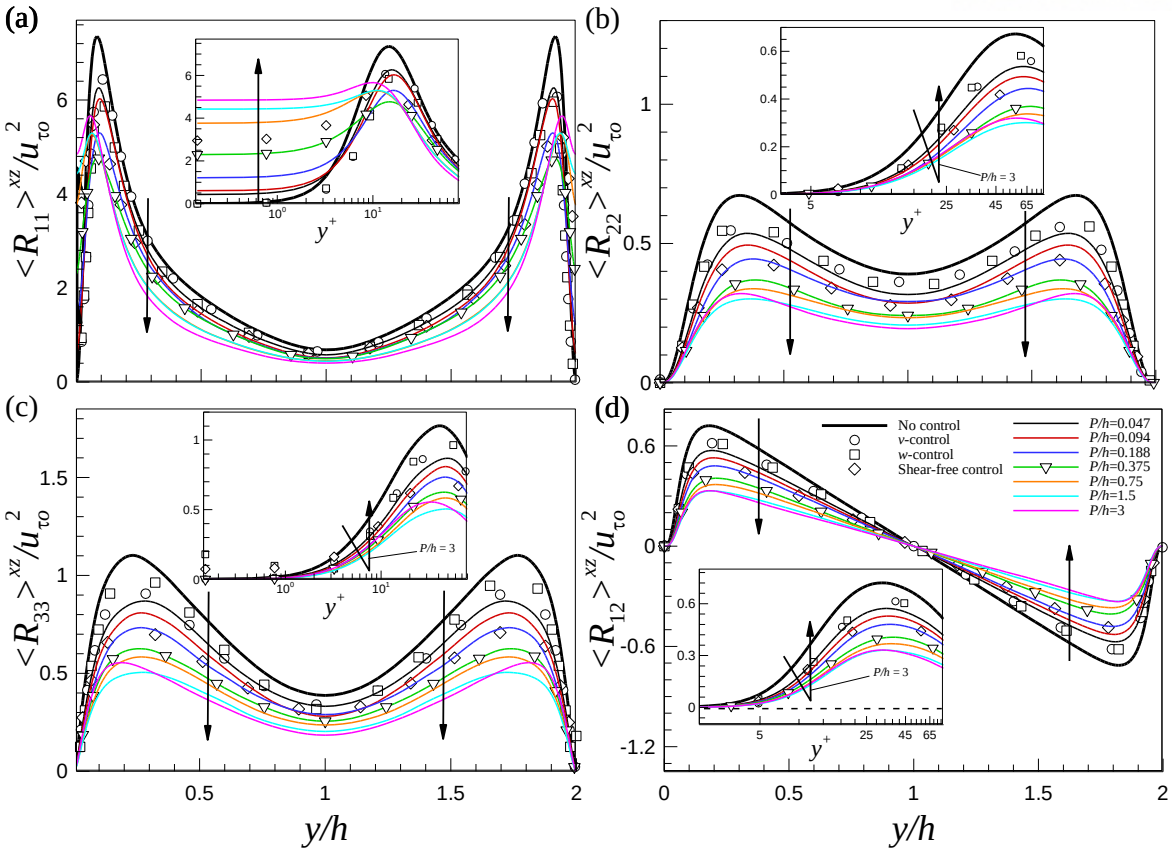

Figure 4. 2 Profiles of turbulent Reynolds stresses with increasing *P/h* for *AR*=0.5 and *A*=1 in the outer coordinates. For *v*- and *w*-controls and shear-free control, *AR*=0.5, *P/h*=0.375 and *A*=1. The insets are logarithmic plots of the Reynolds stresses normalized by $u_{\tau o}$ to clarify near-wall behavior.

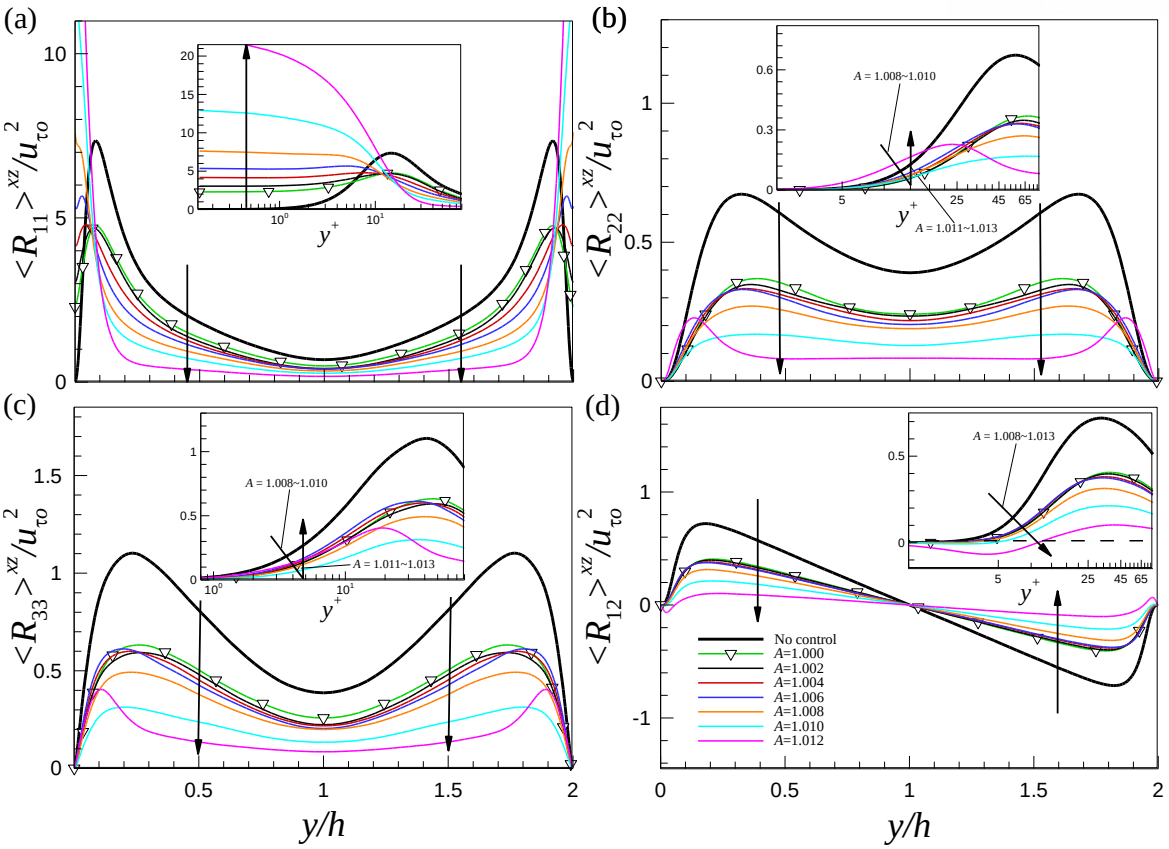

Figure 4. 3 As the same in figure 4.2, but with increasing *A* for *P/h*=0.375 and *AR*=0.5 under the SSFC.

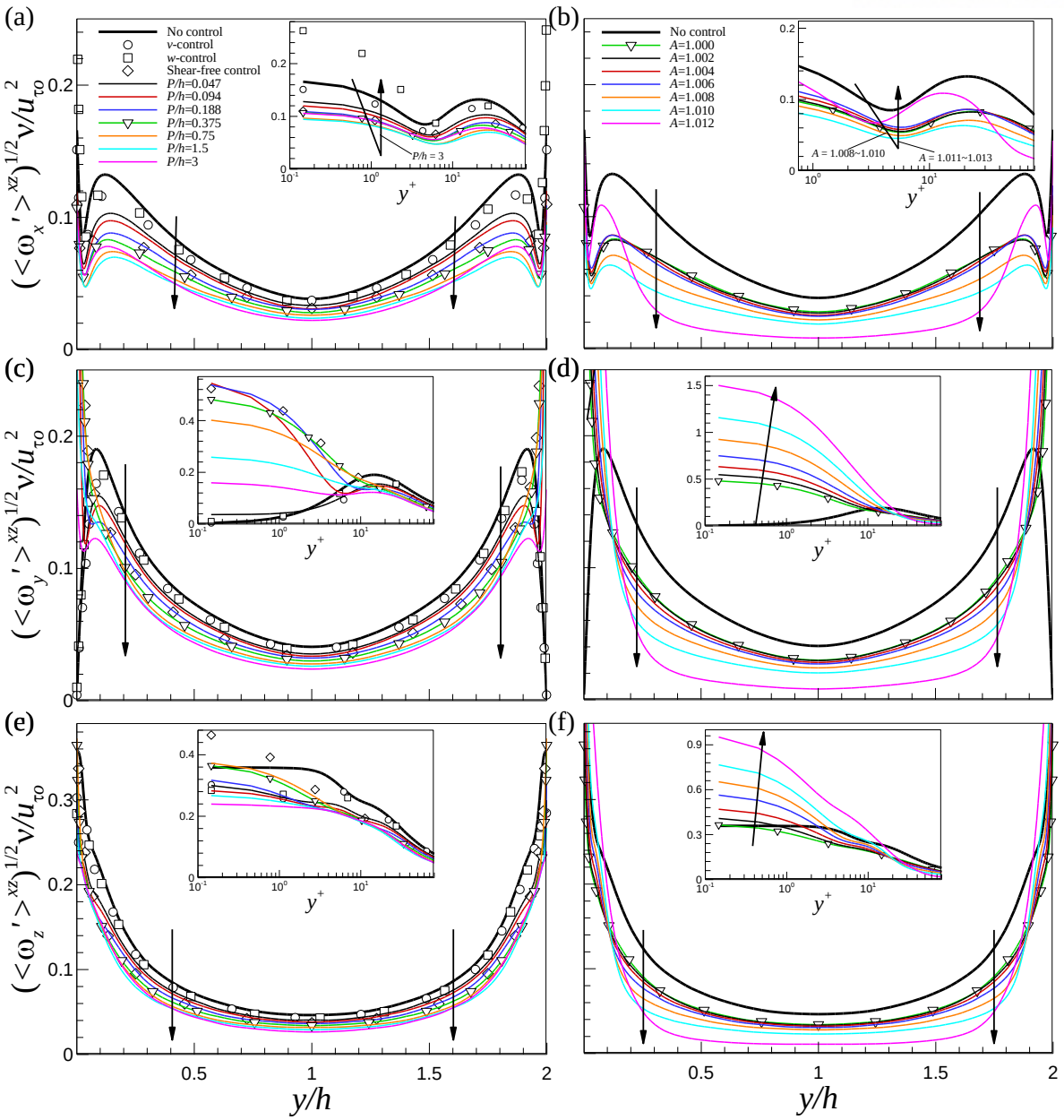

Figure 4. 4 Root-mean-square of vorticity fluctuations normalized by $u_{\tau o}^2 / \nu$ with increasing *P/h* for fixed *AR*=0.5 and *A*=1 (left column) and with increasing *A* for fixed *P/h*=0.375 and *AR*=0.5 (right column). (a, b) streamwise, (c, d) wall-normal, and (e, f) spanwise components. For *v*- and *w*-controls and shear-free control, *P/h*=0.375, *AR*=0.5 and *A*=1. The insets are logarithmic plots in the inner coordinates to clarify near-wall behavior.

5. Turbulent structure

It is well known that the Reynolds shear stress plays a significant role to induce the skin-friction coefficient in canonical wall-bounded turbulent flows [35]. Furthermore, turbulence production and elevated skin-friction drag are closely related with turbulent coherent structures such as quasi-streamwise vortices in the near-wall region and hairpin vortices above the buffer layer [36]. So, reduction of the Reynolds shear stress and skin-friction drag is accompanied by the weakening of related turbulent vortical structures. In this section, to show a clear picture for the relationship between turbulent vortical structures and DR under the SSFC, we analyze modification of turbulent structures based on quadrant analysis, instantaneous view of vortical structures, conditional averaged flow fields and single eddy simulations for autogeneration process of new hairpin vortices.

5.1 Quadrant analysis

The quadrant analysis of the Reynolds shear stress shows the contribution of flow events to the total production (or destruction) of turbulent kinetic energy [23]. In addition, this analysis is used to find the organized structures associated with the bursting event in the canonical turbulent flows [37]. The Reynolds shear stress are separated by signs of u' and v'. Q1, $u' > 0$ and $v' > 0$, indicates outward motion of high-speed fluid; Q2, $u' < 0$ and $v' > 0$, indicates outward motion of low-speed fluid referred to as the ejection events; Q3, $u' < 0$ and $v' < 0$, indicates inward motion of low-speed fluid; Q4, $u' > 0$ and $v' < 0$, indicates an inrush of high-speed fluid referred to as the sweep events.

The contribution of each quadrant scaled by $u_{\tau o}$ is indicated in figure 5.1 as P/h varies for fixed AR=0.5 and A=1 and as A varies for fixed P/h=0.375 and AR=0.5. The sum of the values from the four quadrants (Q1, Q2, Q3 and Q4) is the same to the total mean Reynolds shear stress in figures 4.2(d) and 4.3(d). For the no-control flow (bold solid line), it is indicated the dominance of the Q2 ejection motion away from the wall and the Q4 sweep motion in the very near-wall region, and these motions occupy most of the total mean Reynolds shear stress. In figures 5.1 (a) and (b), it is evident that the Q2 and Q4 events are fairly decreased with increasing P/h far from the wall and the negative contributor to the mean Q1 and Q3 events also becomes smaller under the SSFC. These results show that the reduction of the total mean Reynolds shear stress in figures 4.2(d) is dominantly resulted from large decrease of positive Reynolds shear stress components. Compared with those for P/h=1.5, the second- and fourth-quadrant Reynolds shear stresses for P/h=3 increase in the range of y/h<0.3~0.5, consistent with characteristics in figure 4.2(d), and the first- and third-quadrant components for P/h=3 are slightly reduced throughout the entire wall layer.

In figures 5.1(c) and (d), all of the quadrants far from the wall are fairly reduced as A increases, compared to no-control flow. Four quadrants near the wall have almost similar values at A=1.000~1.007 and are gradually reduced for A≥1.008. However, the Q1 and Q3 components for

y/h<0.1 are enhanced as A increases, contrary to the behavior with varying P/h. Considering the dominance of each quadrant, the Q2 and Q4 event motions are still dominant contributor to the Reynolds shear stress in comparison with Q1 and Q3 events up to A=1.010. However, as A further increases, the dominance of the Q1 and Q3 events is enlarged for A=1.011~1.013, and finally the negative Reynolds shear stresses are more important than the positive Reynolds shear stresses, resulting in the negative Reynolds shear stress profiles in figure 4.3(d) at y^+~25 for A=1.011~1.013. Based on the quadrant analysis, it is concluded that the SSFC with increasing P/h achieve DR by diminishing the positive Reynolds shear stress through the wall layer, whereas that with increasing A not only reduces the positive Reynolds shear stress but also increases the negative Reynolds shear stress for DR.

5.2 Vortical structures

Figures 5.2 and 5.3 indicate iso-surfaces of wall vortical structures visualized using the swirling strength, λ_{ci} obtained as the imaginary part of the complex conjugate eigenvalues [38]. In figures, gray and white regions on the bottom indicate control and no-control surfaces. The modification of the vortical structures under the SSFC with varying P/h for fixed AR=0.5 is indicated in figure 5.2. For the no-control flow, a number of arch-shaped vortices with relatively intense strength are shown in the outer layer and quasi-streamwise vortices are seen to be dominant close to the wall [36]. Two observations can be made from the instantaneous view of the vortical structures under the SSFC. First, the number of vortical structures are gradually reduced as P/h increases. For small P/h, it is evident that the spanwise vortical structures in the outer layer are reduced, and as P/h increases, the quasi-streamwsie vortices near the wall are weakened or suppressed, and the vortices almost disappear over the control surface. Second, even though it is observed that the drag under the SSFC for P/h=3 is slightly smaller than that for P/h=1.5 in figure 3.2, the vortical structures for P/h=3 (figure 5.2f) are more active in the wall layer (y/h<0.5) than those for P/h=1.5, in particular over the no-control surface. For small P/h ($\leq$1.5), the vortical structures over the no-control surface are directly influenced by the control surface, leading to weakening of the vortical structures in the entire domain. However, as P/h exceeds 1.5, the influence of the control surface is not important to affect the vortical structures over the no-control surface. So, quasi-streamwise vortices in the near-wall region and hairpin vortices above the buffer layer over the no-control surface are still dominant, inducing the increase of the wall-normal and spanwise turbulent stresses and Reynolds shear stress for P/h=3 (figure 4.2).

Figure 5.3 indicates iso-surfaces of vortical structures as A increases for fixed AR=0.5 and P/h=0.375. As expected, it is evident that the vortical structures are continuously suppressed as A increase. However, even though the vortical structures for A=1.010 (DR=70%) are totally weakened, new vortical structures in the near-wall region suddenly appear for A=1.011~1.013, particularly over the control surface. Here, the modification of the vortical structures over the no-control and control

surfaces is similar because of small *P/h*. The near-wall vortical structures have been shown in a DNS study of turbulent channel flow using constant near-wall forcing control [39]. They found that when the near-wall forcing is in an optimal condition with the largest DR (70%), there emerge regularly spaced spanwise structures for y^+<20 due to a shear layer in transition.

To provide a proper explanation for the sudden growth of near-wall vortical structures for $A \geq 1.011$, we analyze the advections of the normal vorticity by the spanwise velocity (vortex stretching) and the spanwise vorticity by the wall-normal velocity (vortex transport), which play a significant role in self-sustained mechanism for the near-wall streamwise vortices at low to moderate Reynolds numbers. These two vorticity flux terms are related with the gradient of the Reynolds shear stress. The profiles for two terms are indicated in figure 5.4 as *A* increases for fixed *P/h*=0.375 and *AR*=0.5. The phase-averaged vortex stretching terms are determined as follows:

$$\langle u_3\omega_2 \rangle^{xz} = \frac{1}{2}\left(\langle u_3\omega_2 \rangle^{ns}(y) + \langle u_3\omega_2 \rangle^{cs}(y) \right), \text{where} \tag{5.1}$$

$$\langle u_3\omega_2 \rangle^{ns}(y) = \langle u_3(\boldsymbol{x},t)\omega_2(\boldsymbol{x},t) \rangle^{ns} - \langle u_3(\boldsymbol{x},t) \rangle^{ns} \langle \omega_2(\boldsymbol{x},t) \rangle^{ns} \text{ and}$$

$$\langle u_3\omega_2 \rangle^{cs}(y) = \langle u_3(\boldsymbol{x},t)\omega_2(\boldsymbol{x},t) \rangle^{cs} - \langle u_3(\boldsymbol{x},t) \rangle^{cs} \langle \omega_2(\boldsymbol{x},t) \rangle^{cs}$$

and the phase-averaged vortex transport term is performed in a similar manner. In figure 5.4(a), the absolute vortex stretching term is increasingly enhanced for y^+<10 as *A* increases (<1.011), while it is weakened for y^+>10. Furthermore, the wall-normal location for minimum moves to the wall. However, further increase of *A* ($1.011 \leq A \leq 1.013$) reduces the vortex stretching term for y^+<10 and the minimum moves away from the wall. In figure 5.4(b), it is indicated that the vortex transport term are significantly weakened throughout the whole wall-normal location. On the other hand, sudden increase of the vortex transport term in the range of *A*=1.011~1.1013 are indicated near the wall. The increase of vortex transport term generates increased population of near-wall structures, because the vortex transport is related with generation of near-wall structures from advection of the mean shear by streamwise vorticity [33].

To further analyze relevant vortex dynamics associated with the increased vortex transport term for large *A* near the wall, conditional averaging technique is calculated based on conditional event of spanwise-oriented swirling strength [40, 41, 42]:

$$\left\langle u_j'(\boldsymbol{x}') \,|\, \lambda_{ci}(\boldsymbol{x}) \right\rangle \approx L_j \lambda_{ci}(\boldsymbol{x}), \tag{5.2}$$

where the kernel L_j is determined by minimizing the mean-square error between the estimate and the conditional average. Then,

$$L_j = \frac{\left\langle \lambda_{ci}(\boldsymbol{x}) u_j'(\boldsymbol{x}') \right\rangle}{\left\langle \lambda_{ci}(\boldsymbol{x}) \lambda_{ci}(\boldsymbol{x}) \right\rangle}. \tag{5.3}$$

The estimate of the conditional average is only a function of unconditional two-point correlation data.

Figure 5.5 illustrates estimate of the conditionally averaged velocity field at y_{ref}^{+} =30.3 in the *xy* plane. Closed circle and square indicate centers for the clockwise and counter-clockwise swirling motions respectively and the length of each vector indicates the vector strength. For the no-control flow in figure 5.5(a), a distinct swirling motion with the clockwise rotation is clear because of the induction of hairpin head. On the other hand, figures 5.5(b) and (c) evidently demonstrate that the clockwise spanwise swirling motion is weaker for *A*=1.010 particularly over the control surface, and additional increase of *A* induces strong counter-clockwise motion over the control surface. Over the no-control surface for *A*=1.010, there is only clockwise vortex, while the clockwise and counter-clockwise vortices are coincident for *A*=1.012 because of direct influence of the new counter-clockwise spanwise vortex created over the control surface.

In order to provide a clearer evidence for the rotational sense of the spanwise vortex for *A*=1.012, (*u'*,*v'*) distribution is drawn in figure 5.6 from instantaneous values of *u'* and *v'* at all grid point in the plane. Although the reference wall-normal location for the distribution is chosen here at y_{ref}^{+} =10 due to the strong dominance of the Q2 and Q4 events near the wall for a no-control flow [37] similar characteristic is observed regardless of the wall-normal location. Compared to the no-control flow in figure 5.6(a), it is obvious that slope of solid line over the no-control surface for *A*=1.012 (figure 5.6b) is less inclined to the horizontal direction due to the weakened upward motion (figure 5.5c). Over the control surface in figure 5.6(c), Q1 and Q3 event motions dominantly contribute to the Reynolds shear stress by presence of the near-wall vortices rotating in the opposite direction to spatial signature of hairpin vortex head for a no-control flow in a statistical sense. These results demonstrate that the increase of the wall-normal and spanwise turbulent stresses and streamwise vorticity fluctuations in figures 4.3 and 4.4 for the large *A* is attributed to the generation of the counter-clockwise rotating vortices in the near-wall region.

5.3 Autogeneration

It is widely accepted that hairpins can develop a ‘‘hairpin packet’’ by autogeneration mechanism that is the significant characteristics of turbulent flow, and it has been shown to explain many phenomena in turbulent flow like as significantly much turbulent kinetic energy, many ejection events associated with turbulent bursts, generation of new quasi-streamwise vortex, and characteristic angles of inclined hairpin vortices [38, 43]. Furthermore, the turbulent structure packet is shown to induce a considerable Reynolds shear stress [44], that is divided into two parts: 1) coherent Reynolds stress induced by nonlinear interactions among individual vortices, 2) incoherent stress originated from each individual vortex [43].

In order to judge the robustness of the physical mechanism for the formation of new vortex for a hairpin packet under the SSFC, we analyze autogeneration process of new hairpin vortex. Initially

isolated vortical structures are evolved under the various control parameters, and the initial conditions are acquired by stochastic estimation of conditional averaged flow fields related with Q2 events $\hat{\boldsymbol{u}}(\boldsymbol{x},t=0)=\left\langle \boldsymbol{u}(\boldsymbol{x}) \mid \boldsymbol{u}'(y_{ref})=\alpha \boldsymbol{u}'_{\mathrm{Q2}}(y_{ref}) \right\rangle$ using the DNS data of the control flows as *P/h* and *A* vary. The amplification factor α is defined as the Q2 event strength. Velocity event u'_{Q2} is chosen by detecting the values of $(u',v')=(u_m,v_m)$ that maximize the probability-weighted Reynolds shear stress $u'v'$p.d.f.(u',v') [40]. Figure 5.7 shows examples for the velocity vectors for the no-control and control flows. For the control flows, the largest *P/h* and *A* with maximum DR are considered in (b) and (c). Compared to event angle γ_{II} $(=\tan^{-1}(v_m/u_m))$ for the no-control flow (~33°), that for *A*=1.012 (figure 5.7c) is reduced with maximum DR ~90%, while that for *P/h*=3 (figure 5.7b) is increased with maximum DR ~55%. In previous studies on DR, the event angles are decreased as DR increases [45]. The increase of the angle for *P/h*=3 (~40°) shows that inclination angle of the initial vortex legs is larger that of no-control flow. Although the both values of (u_m,v_m) are decreased compared to those of no-control flow, the event angle γ_{II} for *P/h*=3 is increased because the value of u_m is relatively more decreased than that of v_m. The slight decrease of the angle for *A*=1.012 (~30°) shows that inclination angle of the initial vortex legs is reduced that of no-control flow due to a relatively wide variation of v_m, contrary to that of *P/h*=3. Other cases except for *P/h*=3 and *A*=1.012 have the slightly decreased event angle γ_{II} of 30~32°. The structures extracted by conditional averages for the Q2 events are counter-rotating pairs of streamwise vortices or hairpin vortices, in accordance with the event location (y_{ref}). Because the near-wall variation of the turbulent statistics with increasing *P/h* and *A* was observed for y^+<35~80 in the previous section, the dynamical study for the autogeneration process is performed with two reference locations near the wall (y^+~30) and outer region (y^+~100) in the following.

Figure 5.8 shows evolution of initial vortical structures with α=2 at y^+_{ref} =30.3. The autogeneration process for the no-control flow in figure 5.8(a) is very constant with a previous DNS study [38]. The initial vortical structure evolves into a hairpin-like vortical structure called the primary hairpin vortex (PHV) at t^+=44~62 due to multiple process such as the lift-up of the quasi-streamwise vortices (QSV), generation of the shear layer and roll-up into a spanwise vortex. PHV having Ω-shaped head has been shown since t^+=70 by the self-induced motion toward the binormal direction because of the local effect of the curved vortex line. A secondary hairpin vortex (SHV) at t^+=124 is induced upstream of the primary hairpin vortex (PHV), forming a hairpin vortex packet with an inclination angle ~13° in the outer layer [2000]. It is observed that the vortices move downstream with different convection velocities, because the larger and older hairpin convects faster than the smaller and younger one close to the wall. The spanwise spacing of quasi-streamwise vortex legs maintain approximately 100

viscous wall units, similar to mean low-speed streak spacing [46].

Under the SSFC for P/h=1.5 in figure 5.8(b), it is shown that initial vortex is significantly weakened, and the spanwise spacing of initial vortex at upstream end is larger than that of no-control flow, leading to the decreased Q2 event (figure 5.1). Furthermore, the head component of the initial vortical structure for P/h=1.5 is not connected by a bridge which plays a significant role in the generation of the Ω-shaped vortical structure and SHV. As the initial vortical structure moves downstream with time, the strength is increasingly reduced, and as a result, characteristic Ω-shaped hairpin is not formed whereas there is a little stretching in the streamwise direction because of the mean shear. The initial vortex finally disappear over both the no-control and control surfaces at t^+=186. For P/h=3 (figure 5.8c), the initial vortex over the control surface is very weak and disappears rapidly (t^+=62). Over the no-control surface, however, a Ω-shaped hairpin vortex is observed at a later time than that of no-control flow, and it is found a SHV at t^+=593, although not shown here. The present results indicate that the autogeneration process for new vortical structure over the no-control surface for P/h=3 is valid in the near-wall region, and thus turbulent coherent structures observed in the instantaneous field (figure 5.2) are still active. With increasing amplitude A, in figures 5.8(d) and (e), the initial vortices are obviously weakened, and the autogeneration process for new vortex is totally suppressed over the no-control and control surfaces.

Figure 5.9 indicates evolution of initial vortical structures with α=3 in the outer layer (y^+_{ref} =97.6) as P/h varies. Compared to the process in the near-wall region, it is evident that initial vortical structures spatially develop in the streamwise direction, retaining their integrity, and the PHVs rapidly develop into the characteristic Ω-shaped vortex for all of the cases. In the no-control flow (figure 5.9a), new QSVs are induced at the outer flanks of the primary hairpin vortex legs in response to intense spanwise shearing by legs of the PHV at t^+=186. Although the new QSVs are initially weak and short, these grow rapidly and generate strong rotation [47]. For P/h=0.047~0.75, the Ω-shaped PHV at t^+=124 has a weak kink between the legs of the vortex structure near the junction of the upstream and middle segments, constant with that of the no-control flow (figure 5.9a). After the kink is organized, an intense shear layer rolls up into a compact spanwise vortex structure just above kink to make a new SHV. In this case, however, because the kink is weak and a compact spanwise vortex structure is significantly suppressed, a head of the SHV for P/h=0.047~0.75 is not generated with the weakened lift-up of the SHV. For larger DR in figures 5.9(c) and (d), even though there is a little initial vortices stretching, the SHVs are not formed in upstream and new QSVs are weakened because of the weaken legs of the PHV, showing suppression of the autogeneration process because of the reduced mean shear (figure 4.1b). It is observed that the appearance of the PHVs in the sense of size and shape over the no-control and control surfaces is similar in the outer layer for $P/h \leq 0.375$, suggesting direct interaction of vortical structures over the no-control and control surfaces for small

P/h. However, for large *P/h* ($0.75 \le P/h \le 3$), the streamwise length scale of the PHVs over the no-control surface is longer than that of the control surface because the PHVs over the no-control surface are more stretched by the larger mean shear. The inclination angle of the hairpin vortex legs increases with increasing *P/h* and the spanwise spacings of quasi-streamwise vortex legs are almost constant regardless of *P/h* (≤ 1.5), although it is larger for the control flow than the no-control flow. Figure 5.10 indicates evolution of initial vortices at y_{ref}^{+} =97.6 with varying *A* for fixed *P/h*=0.375 and *AR*=0.5. As similar to the observation in figure 5.9, the autogeneration process of new vortices is significantly weakened and the legs of the PHVs are progressively shortened because of the decreased mean shear. It is observed that for *A*=1, a kink and new QSVs are induced by a strong PHV (figure 5.10b). The appearance of the PHVs in the sense of size and shape is similar over the no-control and control surfaces. For the largest *A*=1.012, neither PHV nor SHV over the no-control and control surfaces is observed.

Figure 5.11 indicates variation of volume averaged Reynolds shear stress. Open and closed symbols show no-control and control surfaces. In figures 5.11(a) and (b), increasing *P/h* and *A* leads to continuous decrease of the volume averaged Reynolds shear stress at y_{ref}^{+} =30.3 because of the weakened autogeneration process and weakened vortices. On the other hand, for the no-control flow, there is a maximum of the normalized Reynolds shear stress at t^{+}=50 because of the organization of the PHV. The decrease of the normalized Reynolds shear stress after t^{+}=50 is due to the largely decaying PHV by continuous outward transfer of the near-wall energy as the structure evolves with time. For small *P/h* (≤ 0.375), the growth rate is similar over the no-control and control surfaces. On the other hand, with increasing *P/h*, the gap of the magnitudes over the no-control and control surfaces is considerable. The largest gap difference of the Reynolds shear stress between no-control and control surfaces is indicated for *P/h*=3 because of active autogeneration process over the no-control surface (figure 5.8c). For *A*=1.012 (DR~90%), the magnitude approaches to nearly zero, because initial vortices totally disappear with time (figure 5.8e). In figure 5.11(c) and (d), the normalized Reynolds shear stresses in the outer layer indicate that magnitude for no-control flow is continuously enhanced with time, distinguishable to that at y_{ref}^{+} =30.3. The increase of the normalized Reynolds shear stress is induced by the continuous growth of the PHV in the outer layer. For the control flows, the Reynolds shear stress are gradually reduced as *P/h* and *A* increase. Furthermore, the difference between the Reynolds shear stresses over the no-control and control surfaces for *P/h*=3 is comparatively small compared to that at y_{ref}^{+} =30.3, because the autogeneration process is not considerably influenced over the no-control and control surfaces (figure 5.9). The normalized Reynolds shear stress for *P/h*=0.047 in the outer layer is quite slowly weakened, inducing relatively small DR.

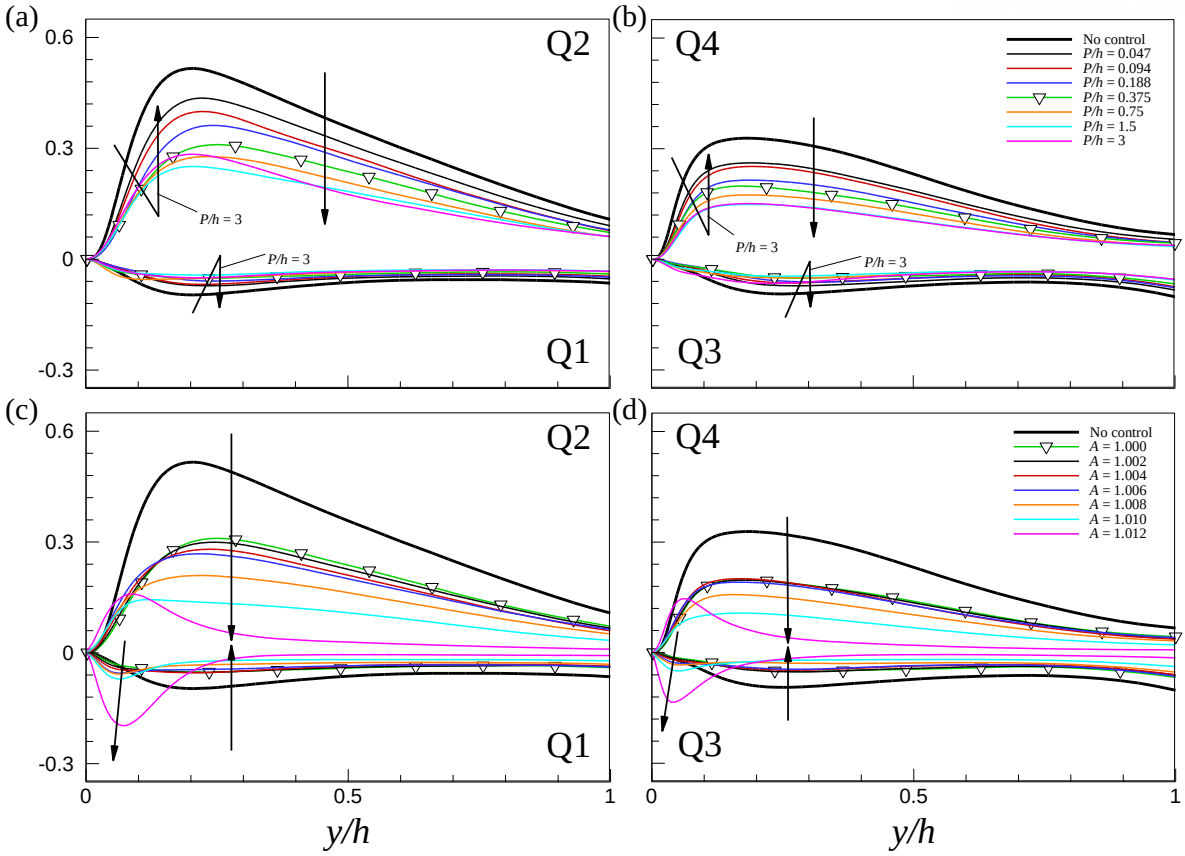

Figure 5. 1 Reynolds shear stress from each quadrant $\langle R_{12} \rangle_{\mathrm{Qi}}^{xz}$ normalized by $u_{\tau o}$ (a, b) with increasing *P/h* for fixed *AR*=0.5 and *A*=1 and (c, d) with increasing *A* for fixed *P/h*=0.375 and *AR*=0.5. The indices i of Qi imply 1, 2, 3 and 4.

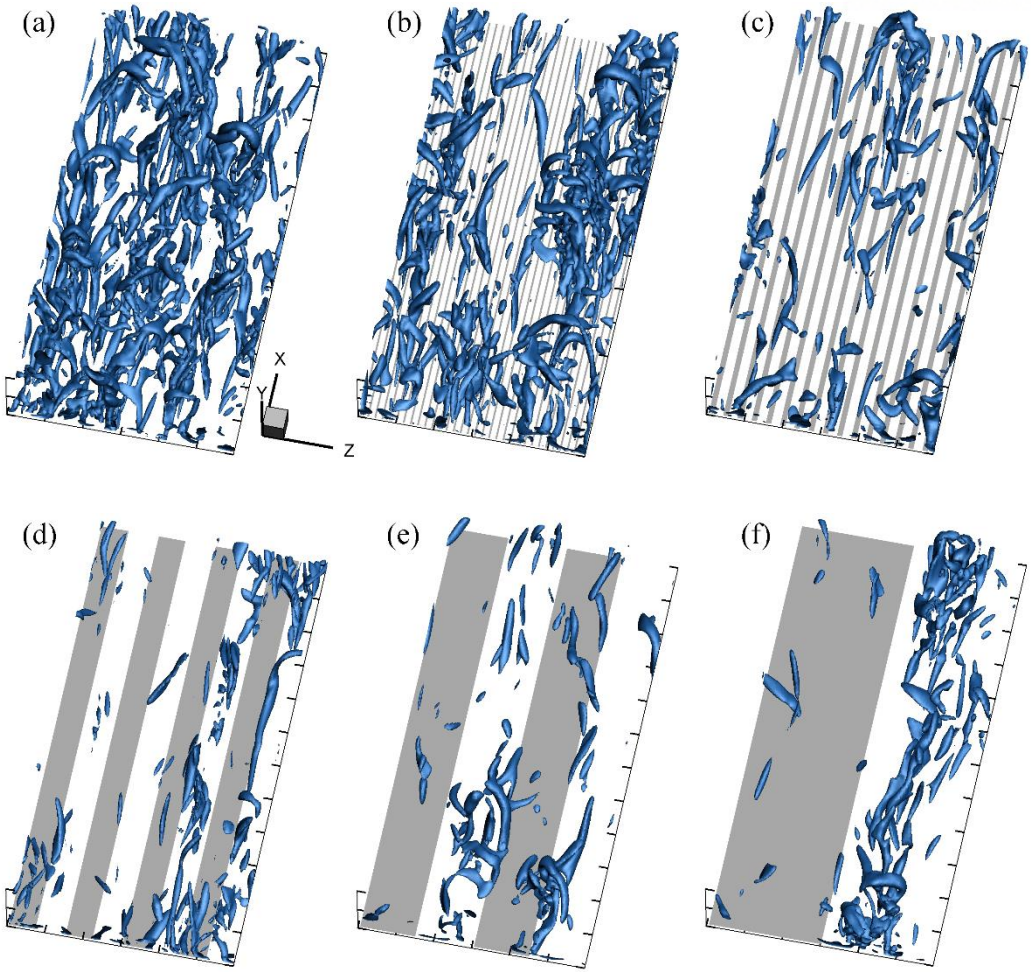

Figure 5. 2 Visualization of vortical structures in turbulent channel flows under the SSFC with varying *P/h* for *AR*=0.5. (a) no-control flow, (b) *P/h*=0.094, (c) *P/h*=0.188, (d) *P/h*=0.75, (e) *P/h*=1.5 and (f) *P/h*=3. The distance of ticks is 0.5*h*. The contour is normalized by U_c/h and the contour of 17% of the maximum λ_{ci} is employed to depict the structures. The grey and white colors on the bottom indicate control and no-control surfaces.

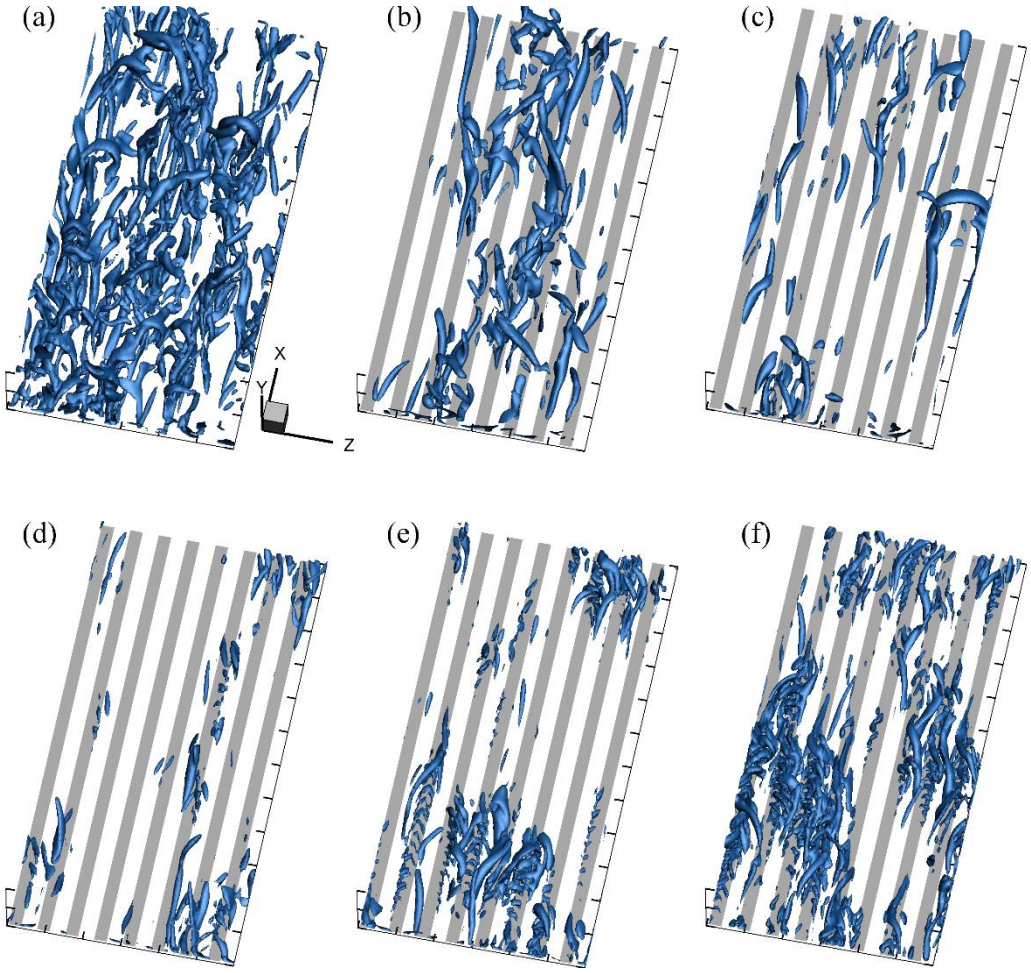

Figure 5. 3 As the same in figure 5.2, but for *P/h*=0.375 and *AR*=0.5 as a function of amplitude *A*. (a) no-control flow, (b) *A*=1.000, (c) *A*=1.008, (d) *A*=1.010, (e) *A*=1.011 and (f) *A*=1.012.

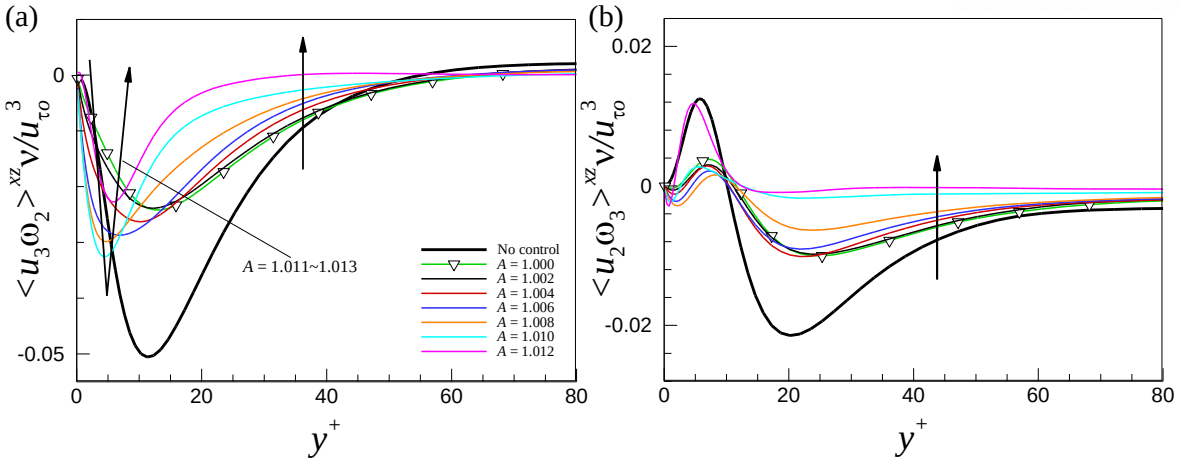

Figure 5. 4 Inner-scaled (a) vortex stretching term and (b) vortex transport term with increasing *A* for fixed *P/h*=0.375 and *AR*=0.5.

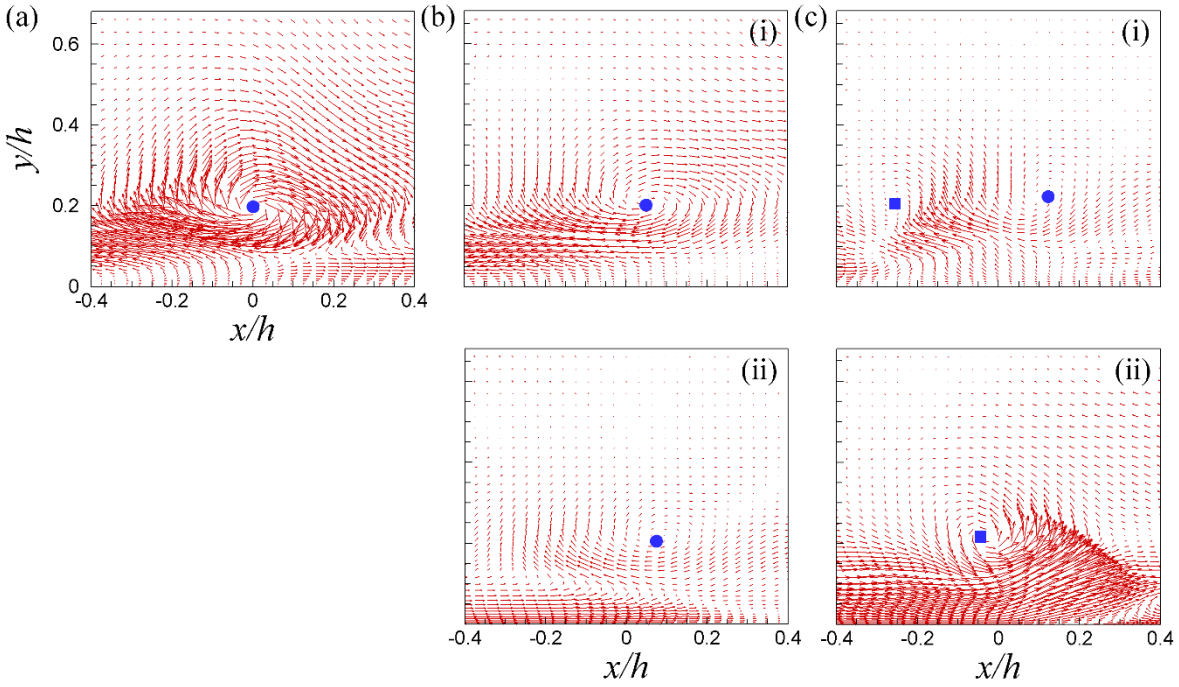

Figure 5. 5 Linear stochastic estimation of $<u_j'(x')|\lambda_{ci}(x)>$ at y_{ref}^+ =30.3. Closed circle and square indicate the clockwise and counter-clockwise rotating vortices respectively. (a) no-control flow, (b,c) control flows: (b) *A*=1.010 and (c) *A*=1.012. (i) no-control surface and (ii) control surface. In (b) and (c), *P/h*=0.375 and *AR*=0.5.

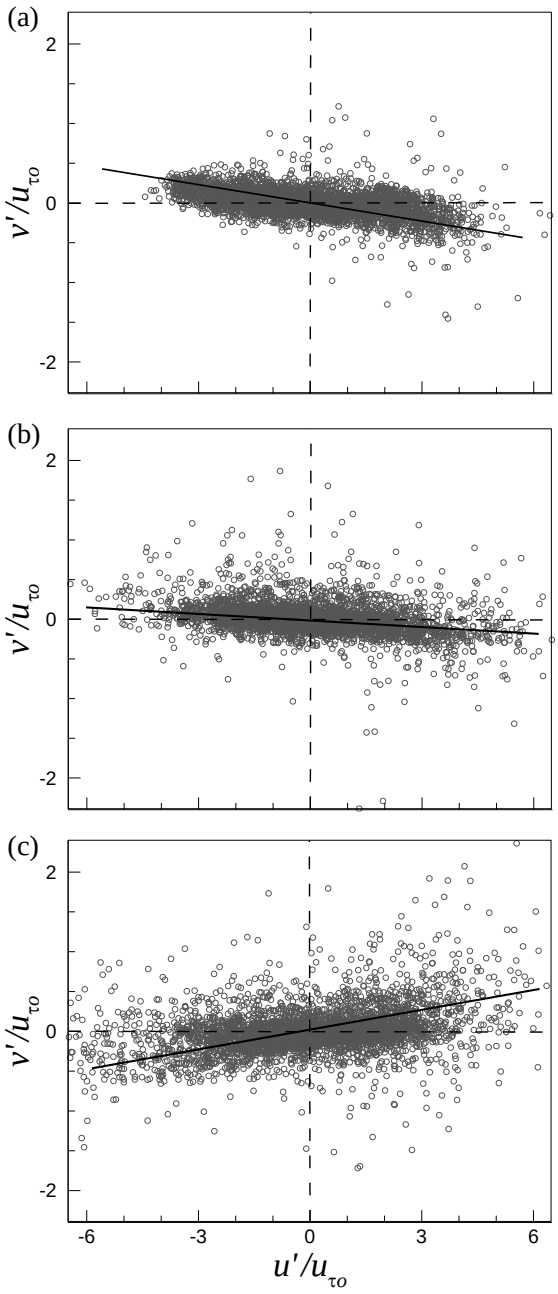

Figure 5. 6 Distribution of (*u*′,*v*′) at y^+_{ref} =10. (a) no-control flow and (b, c) control flow for *A*=1.012, *P/h*=0.375 and *AR*=0.5: (b) no-control surface and (c) control surface.

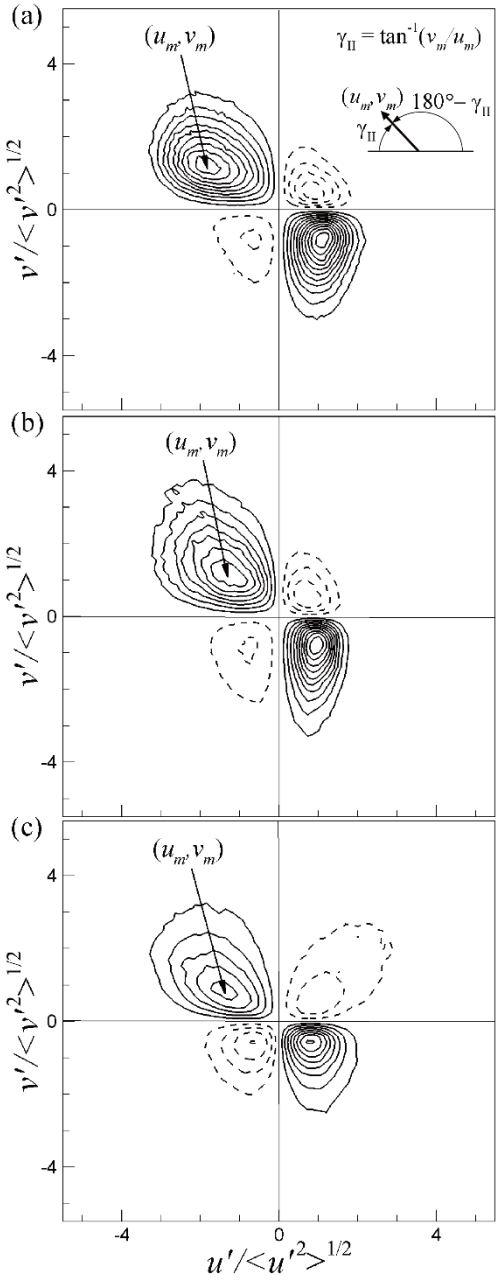

Figure 5. 7 Probability weighted Reynolds shear stress *u′ v′*p.d.f.(*u′*,*v′*) at y^+_{ref} =30.3. (a) no-control flow, (b) control flow for *P/h*=3, *AR*=0.5 and *A*=1 and (c) control flow for *P/h*=0.375, *AR*=0.5 and *A*=1.012. Here, $u_i^{'}$ is the velocity stochastic component and $\langle \cdot \rangle$ indicates time- and streamwise-averaged quantities.

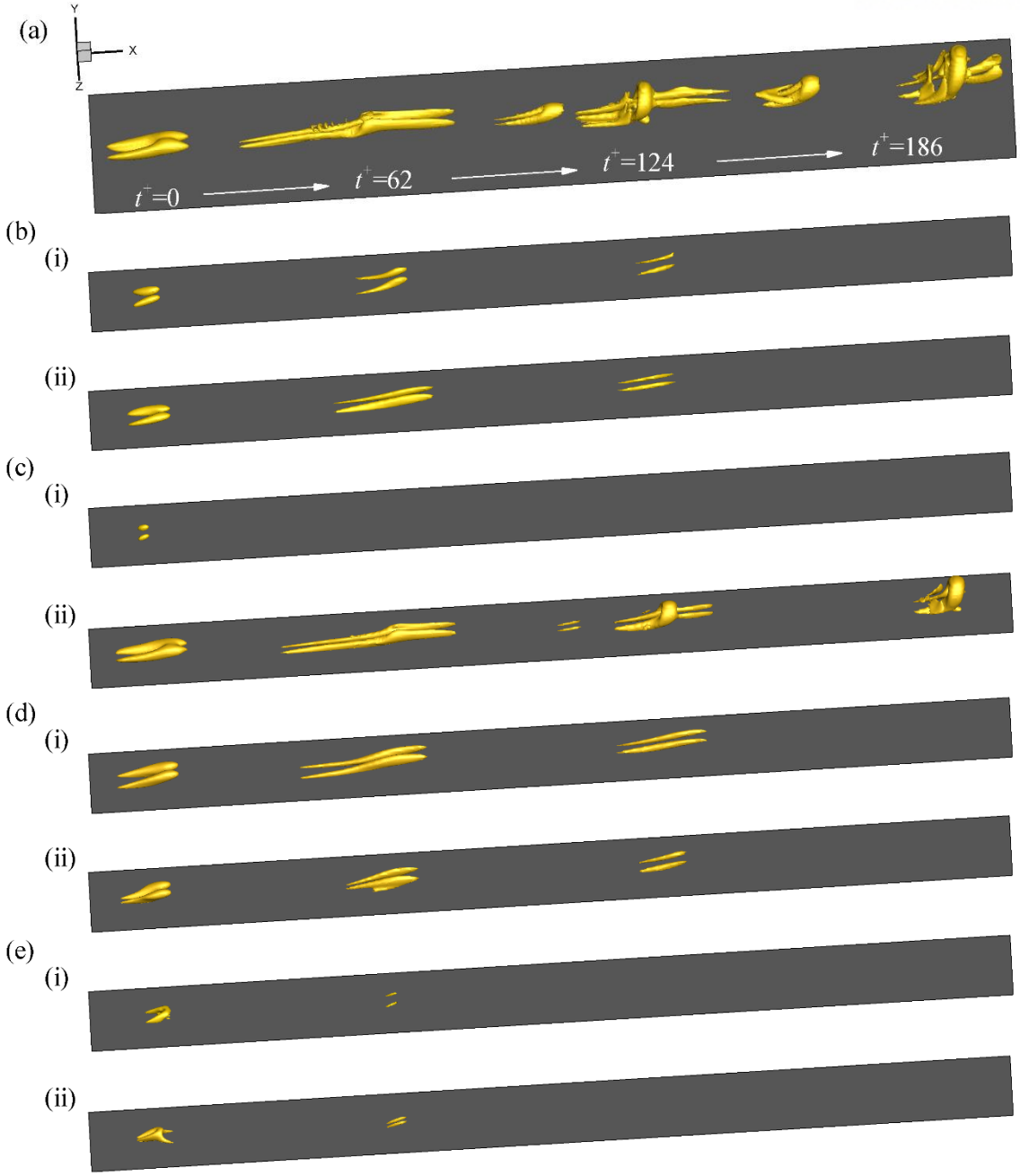

Figure 5. 8 The evolution of initial vertical structure extracted by Q2 event vector of strength α=2 at y^+_{ref} =30.3. Vortices are shown using the isosurfaces of 25% of the maximum swirling strength (λ_{ci}) of the initial eddy: (a) no-control flow and (b-e) control flows: (b) *P/h*=1.5, (c) *P/h*=3, (d) *A*=1.008 and (e) *A*=1.012. (i) and (ii) indicate control and no-control surfaces. In (b) and (c), *AR*=0.5 and *A*=1 and in (d) and (e), *P/h*=0.375 and *AR*=0.5.

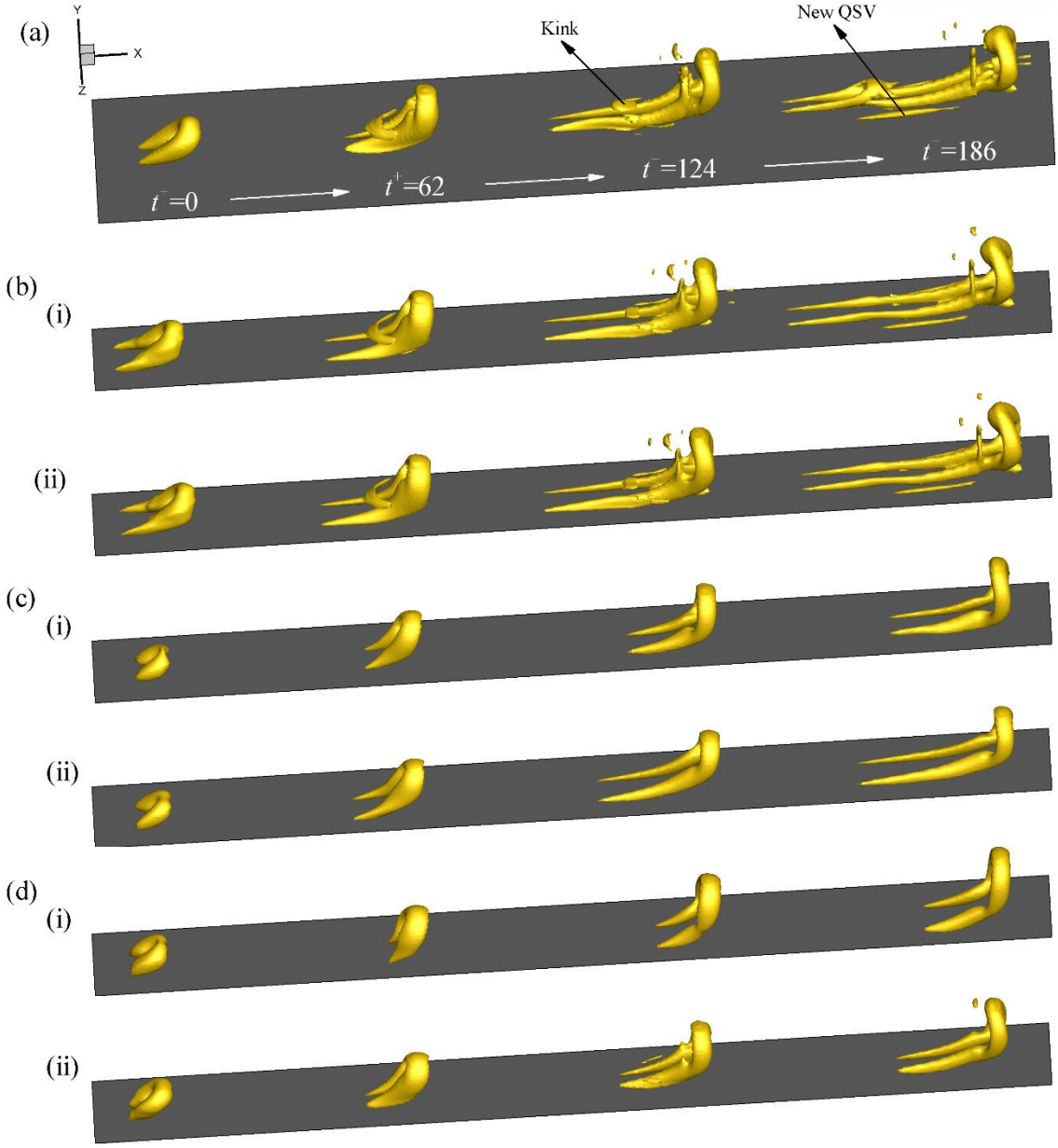

Figure 5. 9 The evolution of initial vertical structure extracted by Q2 event vector of strength α=3 at y^+_{ref} =97.6. Vortices are shown using the isosurfaces of 30% of the maximum swirling strength (λ_{ci}) of the initial eddy. (a) no-control flow and (b-d) control flows: (b) *P/h*=0.047, (c) *P/h*=1.5 and (d) *P/h*=3. (i) and (ii) indicate control and no-control surfaces. For (b-d), *AR*=0.5 and *A*=1.

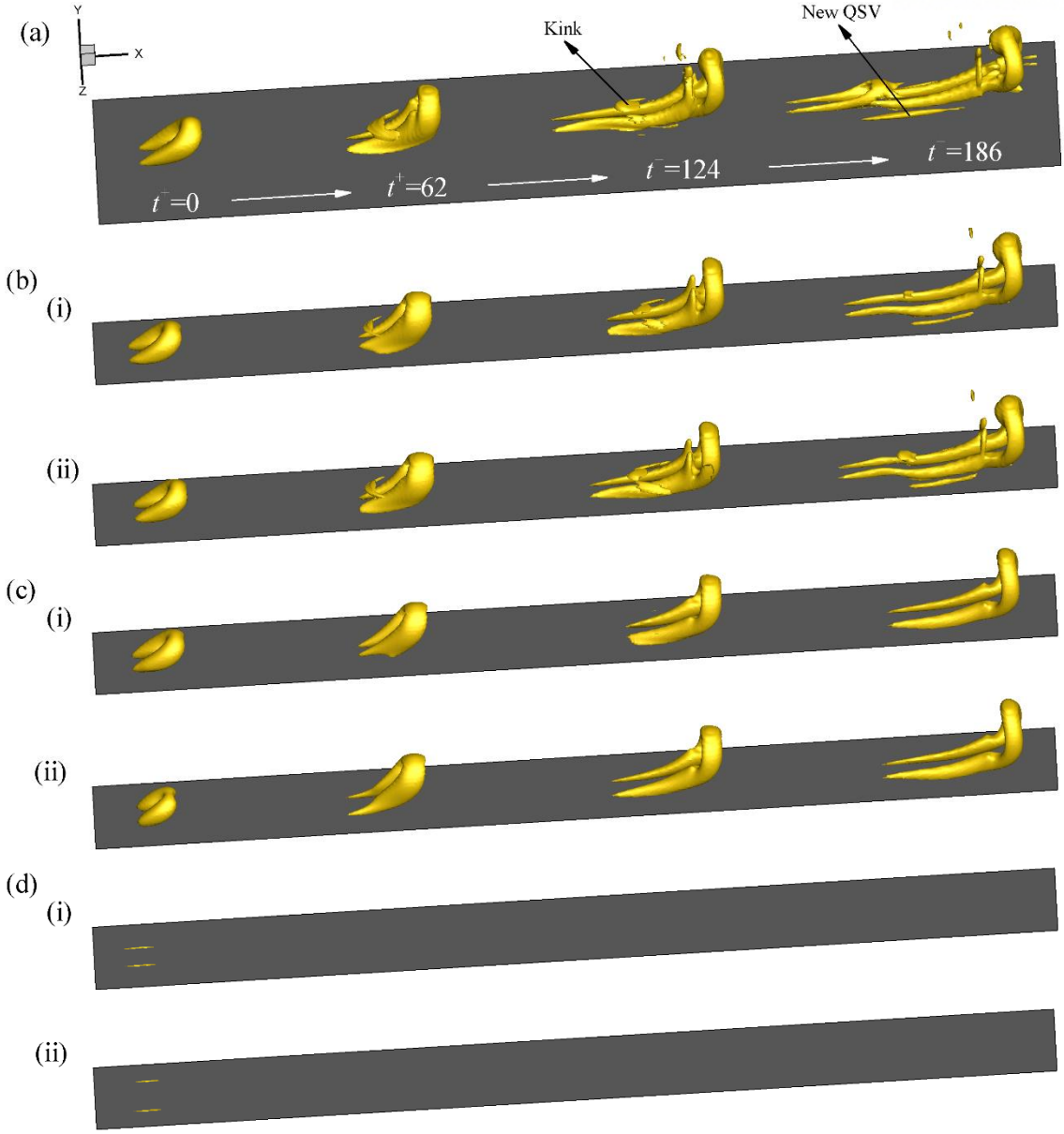

Figure 5. 10 The evolution of initial vertical structure extracted by Q2 event vector of strength α=3 at y^+_{ref} =97.6. Vortices are shown using the isosurfaces of 30% of the maximum swirling strength (λ_{ci}) of the initial eddy. (a) no-control flow and (b-d) control flows: (b) A=1.000, (c) A=1.008 and (d) A=1.012. (i) and (ii) indicate control and no-control surfaces. In (b-d), P/h=0.375 and AR=0.5.

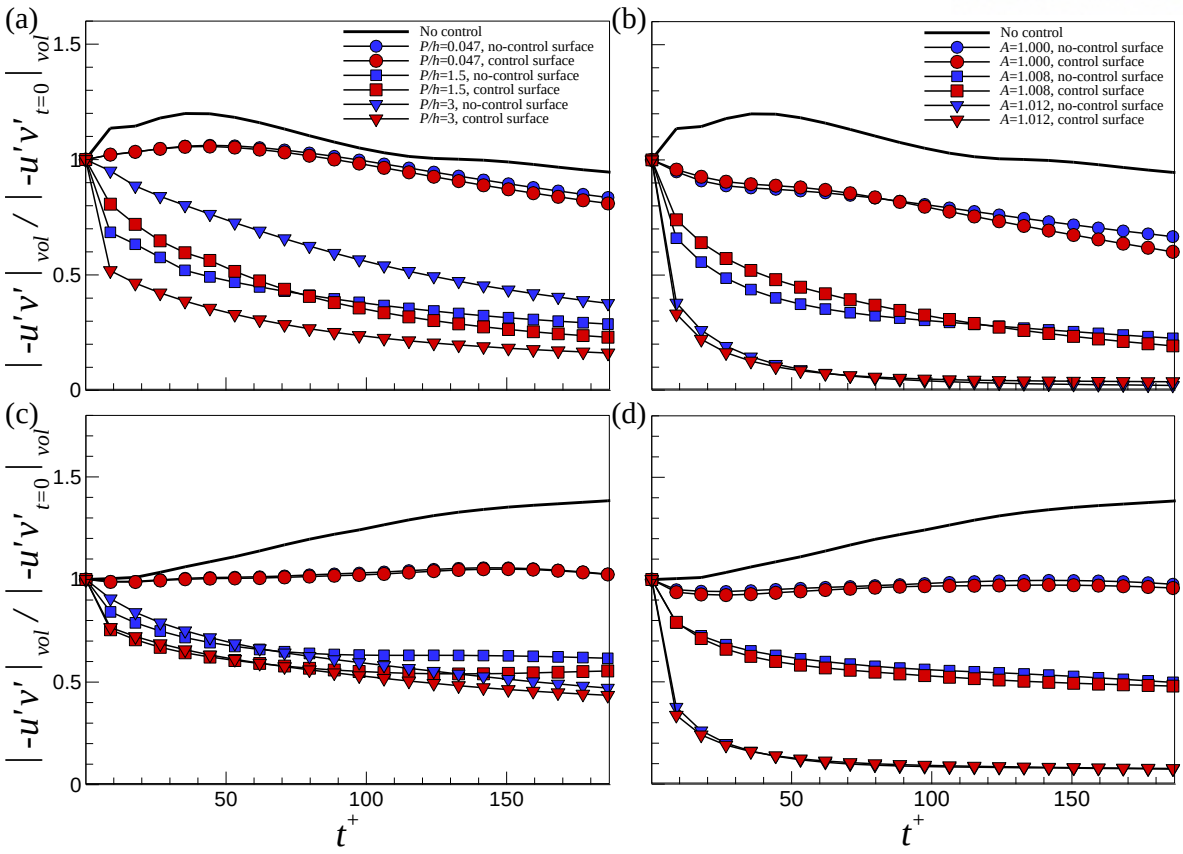

Figure 5. 11 The volume averaged Reynolds shear stress $|-u'v'|$ scaled by its initial value during evolution of the initial structures extracted by Q2 event vector with increasing (a) *P/h* with α=2 at y^+_{ref} =30.3, (b) *A* with α=2 at y^+_{ref} =30.3, (c) *P/h* with α=3 at y^+_{ref} =97.6 and (d) *A* with α=3 at y^+_{ref} =97.6.

6. Summary and conclusions

We conducted DNSs of turbulent channel flows to apply a closed-loop active control concept for DR using streamwise wall-shear free control (SSFC) at $Re_{\tau o}$=180. Both channel walls consisted of spanwise-alternating no-control and control surfaces as *P/h* varies. In order to increase the skin-friction DR, we applied an amplitude parameter (*A*) for the strength of actuating streamwise velocity at the wall. Compared with previous studies of closed-loop active control schemes throughout the entire wall (*v*- and *w*-controls with 20-25% DR [3], suboptimal control with 16-22% DR [4, 5] and control with detection of the near-wall streamwise vortices with 11-16% DR [6], we found that the maximum DR is as high as 90% under the SSFC, while the control was applied only to half of the entire domain. An inspection of the mean velocity profiles indicated that the mean velocity shear clearly decreases as *P/h* and *A* increase. Furthermore, with increasing DR, the mean velocity profiles were more largely shifted upward without modification of the slope for the log-law, consistent with previously studied drag-reducing flows. Regarding the Reynolds stresses, all of the magnitudes in the outer layer decreased continuously as *P/h* and *A* increase, inducing the maximum DR for the largest values of *P/h* and *A*. In the near-wall region, however, the streamwise normal stress was decreased as *P/h* and *A* increase because of the streamwise velocity input. Furthermore, even though continuous reductions of the wall normal and spanwise normal stresses and Reynolds shear stress were observed for small values of *P/h* and *A*, a additional increase in the parameters resulted in an increase in the statistics. The near-wall Reynolds shear stress became negative for a large value of *A*. Consistent behavior in the outer layer with increases in *P/h* and *A* was also observed in the vorticity fluctuations, while the near-wall characteristics were slightly complex. In terms of energy efficiency, increasing the amplitude parameter *A* with fixed values of *P/h* deteriorated the net energy savings rate. The maximum net energy savings rates with fixed values of *P/h* and *AR* were observed with the largest values of *P/h* (~56.8%) and *AR* (~83.8%) respectively, when *A*=1.002 and 1.001, showing that as the control area increases, the energy efficiency increases with the optimal values of the forcing parameter. On the other hand, increasing the control area requires many sensors and actuators at the wall, thus complicating the hardware system due to overloads.

The modification of the turbulent coherent structures related with the Reynolds shear stress was documented to give not only an explanation of the change of the turbulent statistics but also to give the DR mechanism under the SSFC. The quadrant analysis indicated that the dramatic reduction of the Reynolds shear stress with increasing *P/h*, leading to considerable skin-friction DR, can be attributed to the weakness of Q2 and Q4 events through the wall layer, while this decrement with an increase in *A* results from both the decrement of the positive Reynolds shear stress and the increment of the negative Reynolds shear stress. The decrement of the Q2 and Q4 events was accompanied by the weakening of the quasi-streamwise vortices in the near-wall region and hairpin vortices above the

buffer layer. The enhancement in the Reynolds shear stress for a large *P/h* in the near-wall region was induced by the active turbulent structures residing over the no-control surface, although the vortical structures over the control surface were considerably weakened. The autogeneration process for a new vortex was found to play a significant role in activating the near wall coherent structures over the no-control surface for a large *P/h*, inducing active Q2and Q4 event motions with an intense shear layer. However, the increased negative Reynolds shear stress for a large *A* was confirmed to be created by the enhanced vortex transport term, which is closely related with the generation of the near-wall vortices from the advection of the mean shear by the streamwise vorticity. The conditional averaged flow fields with a spanwise swirling event indicated that the newly generated near-wall vortices over the control surface for a large *A* rotate in a counter-clockwise direction that is opposite to the spatial signature of a hairpin vortex head for a no-control flow in a statistical sense. Furthermore, the autogeneration process for a new vortex was completely suppressed when *A* was varied. As a result, Q1 and Q3 events mostly contributed to inducing negative Reynolds shear stress for a large *A*. In the outer layer, the autogeneration process of new vortices was significantly weakened regardless of *P/h* and *A* due to the less considerable streamwise-stretching and the decreased vortices, although the dynamical interaction of the vortical structure for a small *P/h* was constant with that for a no-control flow.

It is worth mentioning that underlying DR mechanism proposed above is applicable to turbulent channel flows with SHSs using a shear-free condition at the wall. When the shear-free condition in the streamwise and spanwise directions at wall is applied to an initial vortical structure, the additional shear-free condition in the spanwise direction enhances the vortical structure over time, while a new vertical structure in the upstream directions is not spawned by the autogeneration process (figure 6.1). The greater stretching of the vortices under the shear-free control in (b) and (d) indicates the induction of more drag than that under the SSFC, consistent with the greater magnitude of the Reynolds stresses under shear-free control compared to those under the SSFC.

Finally, it is extremely difficult to install many small-scale sensors and actuators over a wide range of wall area in real experiments. Nevertheless, an active flow control concept for DR provides useful information for how wall turbulence responds to the input condition with structural modification to devise an effective active flow control strategy in future.

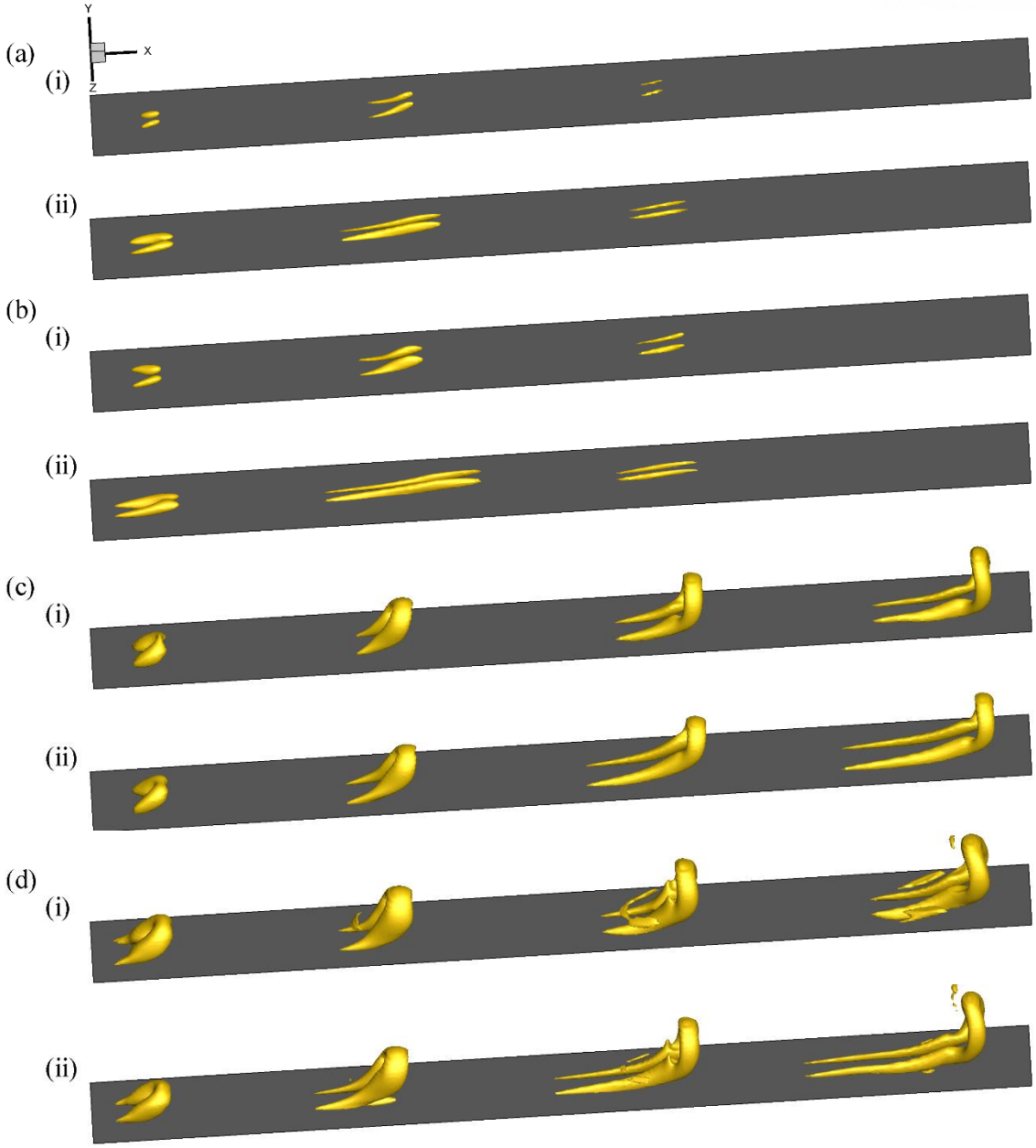

Figure 6. 1 The evolution of initial vertical structure extracted by Q2 event vector of strength α=2 and 3 at y^+_{ref} =30.3 (a, b) and 97.6 (c, d). Structures indicate iso-surfaces of 25% and 30% of the maximum swirling strength λ_{ci} respectively: (a, c) SSFC and (b, d) shear-free control. (i) and (ii) indicate control and no-control surfaces. In (a-d), *P/h*=1.5, *AR*=0.5 and *A*=1.

REFERENCES

1. Kasagi, N., Hasegawa, Y. & Fukagata, K. 2009 Toward cost-effective control of wall turbulence for skin-friction drag reduction. *In Advances in Turbulence XII*. **132**, 189-200. Springer.

2. Kim, J. & Bewley, T. R. 2007 A linear systems approach to flow control. *Annu. Rev. Fluid Mech.* **39**, 383-417.

3. Choi, H., Moin, P. & Kim, J. 1994 Active turbulence control for drag reduction in wall-bounded flows. *J. Fluid Mech.* **262**, 75-110.

4. Bewley, T. R. & Moin, P. 1994 Optimal control of turbulent channel flow for reduction of pressure fluctuations. In *Active Control of Vibration and Noise* (ed. K. W. Wang *et al*.) ASME DE-Vol. 75.

5. Lee, C., Kim, J. & Choi, H. 1998 Suboptimal control of turbulent channel flow for drag reduction. *J. Fluid Mech.* **358**, 245-258.

6. Ge, M., Xu, C. & Cui, G. X. 2015 Active control of turbulence for drag reduction based on the detection of near-wall streamwise vortices by wall information. *Acta Mechanica Sinica*, vol. 31, pp. 512-522. Springer.

7. Min, T., Kang, S. M., Speyer, J. L. & Kim, J. 2006 Sustained sub-laminar drag in a fully developed channel flow. *J. Fluid Mech.* **558**, 309-318.

8. Kim, K. & Sung, H. J. 2006 Effects of unsteady blowing through a spanwise slot on a turbulent boundary layer. *J. Fluid Mech.* **557**, 423-450.

9. Quadrio, M., Ricco, P. & Viotti, C. 2009 Streamwise-travelling waves of spanwise wall velocity for turbulent drag reduction. *J. Fluid Mech.* **627**, 161-178.

10. Chung, Y. M. & Sung, H. J. 2003 Sensitivity study of turbulence control with wall blowing and suction. *Turbulence and Shear Flow Phenomena-3: Third International Symposium on Turbulence and Shear Flow Phenomenon Sendai*. Vol. 1, PP. 167-172.

11. Chung, Y. M. & Talha, T. 2011 Effectiveness of active flow control for turbulent skin friction

drag reduction. *Phys. Fluids* **23**, 025102.

12. Koumoutsakos, P. 1999 Vorticity flux control for a turbulent channel flow. *Phys. Fluids* **11**, 248-250.

13. Quadrio, M. & Ricco, P. 2004 Critical assessment of turbulent drag reduction through spanwise wall oscillation. *J. Fluid Mech.* **521**, 251-271.

14. Lumley, J. L. 1969 Drag reduction by additives. *Ann. Rev. Fluid Mech.* **1**, 367-384.

15. Choi, H., Moin, P. & Kim, J. 1993 Direct numerical simulation of turbulent flow over riblets. *J. Fluid Mech.* **255**, 503-539.

16. Hahn, S., Je, J. & Choi, H. 2002 Direct numerical simulation of turbulent channel flow with permeable walls. *J. Fluid Mech.* **450**, 259-285.

17. Min, T. & Kim, J. 2004 Effect of superhydrophobic surfaces on skin-friction drag. *Phys. Fluids* **16**, L55.

18. Martell, M. B., Rothstein, J. P. & Perot, J. B. 2010 An analysis of superhydrophobic turbulent drag reduction mechanisms using direct numerical simulation. *Phys. Fluids* **22**, 065102.

19. Park, H., Park, H. & Kim, J. 2013 A numerical study of the effects of superhydrophobic surface on skin-friction drag in turbulent channel flow. *Phys. Fluids* **25**, 110815.

20. Rastegari, A. & Akhaban, R. 2015 On the mechanism of turbulent drag reduction with super-hydrophobic surfaces. *J. Fluid Mech.* **773**, R4.

21. Jung, T., Choi, H. & Kim, J. 2016 Effects of the air layer of an idealized superhydrophobic surface on the slip length and skin-friction drag. *J. Fluid Mech.* **790**, R1.

22. Philip, J. R. 1972 Flows satisfying mixed no-slip and no-shear conditions. *Z. Angew. Math. Phys.* **23**, 353-372.

23. Wallace, J. M. 2016 Quadrant Analysis in Turbulence Research: History and Evolution. *Annu. Rev. Fluid Mech.* **48**, 131–158.

24. Jelly, T. O., Jung, S. Y. & Zaki, T. A. 2014 Turbulence and skin friction modification in channel flow with streamwise-aligned superhydrophobic surface texture. *Phys. Fluids* **26**, 095102.

25. Turk, S., Daschiel, G., Stroh, A., Hasegawa, Y. & Frohnapfel, B. 2014 Turbulent flow over superhydrophobic surfaces with streamwise grooves. *J. Fluid Mech.* **747**, 186-217.

26. Perkins, R. M. 2014 PIV Measurements of Turbulent Flow in a Rectangular Channel over Superhydrophobic surfaces with Riblets. *All Theses and Dissertations.* Paper 5547.

27. Seo, J., Garcia-Mayoral, R. & Mani, A. 2015 Pressure fluctuations and interfacial robustness in turbulent flows over superhydrophobic surfaces. *J. Fluid Mech.* **783**, 448–473.

28. Lee, C. & Kim, C.-J. 2011 Underwater restoration and retention of gases on superhydrophobic surfaces for drag reduction. *Phys. Rev. Lett.* **106**, 014502.

29. Park, H., Sun, G. & Kim, C.-J. 2014 Superhydrophobic turbulent drag reduction as a function of surface grating parameters. *J. Fluid Mech.* **747**, 722–734.

30. Sun, G., Park, H. & Kim, C.-J. 2015 Development of a Miniature Shear Sensor for Direct Comparison of Skin-Friction Drags. *J. MicroElectroMechan. Syst.* **24**, 1426-1435.

31. Kim, K., Baek, S.-J. & Sung, H. J. 2002 An implicit velocity decoupling procedure for the incompressible Navier-Stokes equations. *Intl J Numer Meth Fluids* **38**, 125-138.

32. Reynolds, W. C. & Hussain, A. K. M. F. 1972 The mechanics of an organized wave in turbulent shear flow. Part 3. Theoretical models and comparisons with experiments. *J. Fluid Mech.* **54**, 263–288.

33. Jimenez, J. & Pinelli, A. 1999 The autonomous cycle of near-wall turbulence. *J. Fluid Mech.* **389**, 335–359.

34. Suzuki, Y. & Kasagi, N. 1992 Evaluation of hot-wire measurements in wall shear turbulence using a direct numerical simulation database. *Exps. Thermal Fluid Sci*. **5**, 69–77.

35. Fukagata, K., Iwamoto, K. & Kasagi, N. 2002 Contribution of Reynolds stress distribution to the skin friction in wall-bounded flows. *Phys. Fluids* **14**, L73–L76.

36. Adrian, R. J. 2007 Hairpin vortex organization in wall turbulence. *Phys. Fluids* **19**, 041301.

37. Kim, J., Moin, P. & Moser, R. 1987 Turbulence statistics in fully developed channel flow at low Reynolds number. *J. Fluid Mech.* **177**, 133–166.

38. Zhou, J., Adrian, R. J., Balachandar, S. & Kendall, T. M. 1999 Mechanisms for generating coherent packets of hairpin vortices. *J. Fluid Mech.* **387**, 353–396.

39. Xu, J., Dong, S., Maxey, M. R. & Karniadakis, G. E. 2007 Turbulent drag reduction by constant near-wall forcing. *J. Fluid Mech.* **582**, 79-101.

40. Adrian, R. J. 1996 Stochastic estimation of the structure of turbulent fields. In *Eddy Structure Identification* (ed. J. P. Bonnet), pp. 145–196. Springer.

41. Christensen, K. T. & Adrian, R. J. 2001 Statistical evidence of hairpin vortex packets in wall turbulence. *J. Fluid Mech.* **431**, 433–443.

42. Lee, J. H. & Sung, H. J. 2011 Very-large-scale motions in a turbulent boundary layer. *J. Fluid Mech.* **673**, 80–120.

43. Adrian, R. J., Meinhart, C. D. & Tomkins, C. D. 2000 Vortex organization in the outer region of the turbulent boundary layer. *J. Fluid Mech.* **422**, 1–54.

44. Ganapathisubramani, B., Longmire, E. K. & Marusic, I. 2003 Characteristics of vortex packets in turbulent boundary layers. *J. Fluid Mech.* **478**, 35–46.

45. Kim, K., Li, C., Sureshkumar, R., Balachandar, S. & Adrian, R. 2007 Effects of polymer stress on eddy structures in drag-reduced turbulent channel flow. *J. Fluid Mech.* **584**, 281-299.

46. Kline, S. J., Reynolds, W. C., Schraub, F. A. & Rundstadler, P. W. 1967 The structure of turbulent boundary layers. *J. Fluid Mech.* **30**, 741–773.

47. Bernard, P. S., Thomas, J. M. & Handler, R. A. 1993 Vortex dynamics and the production of Reynolds stress. *J. Fluid Mech.* **253**, 385-419.